

¹ Susceptible host dynamics explain pathogen resilience to
² perturbations

⁴
⁵ Sang Woo Park, . . . , Bryan T. Grenfell, Sarah Cobey

⁶ Abstract

⁷ Major priority for epidemiological research in the time of anthropogenic change is
⁸ understanding how infectious disease dynamics respond to perturbations. Interven-
⁹ tions to slow the spread of SARS-CoV-2 significantly disrupted the transmission
¹⁰ of other human pathogens. As interventions lifted, whether and when respiratory
¹¹ pathogens would eventually return to their pre-pandemic dynamics remains to be
¹² answered. Here, we present a framework for estimating pathogen resilience based
¹³ on how fast epidemic patterns return to their pre-pandemic, endemic dynamics. By
¹⁴ analyzing time series data from Hong Kong, Canada, Korea, and the US, we quan-
¹⁵ tify the resilience of common respiratory pathogens and provide predictions about
¹⁶ when each pathogen will eventually return to their pre-pandemic, endemic dynamics.
¹⁷ Our predictions about whether each pathogen should have already returned to their
¹⁸ pre-pandemic dynamics closely match the observed patterns of deviations (or lack
¹⁹ thereof) from their pre-pandemic dynamics. Finally, we show that the replenishment
²⁰ rate of the susceptible pool is a key determinant of pathogen resilience, which in turn
²¹ determines the persistence of the pathogen.

Non-pharmaceutical interventions (NPIs) to slow the spread of SARS-CoV-2 disrupted the transmission of other human respiratory pathogens, adding uncertainties to their future epidemic dynamics and the overall public health burden [1]. As NPIs lifted, large heterogeneities in outbreak dynamics were observed across different pathogens in different countries, with some pathogens exhibiting earlier resurgences than others [2, 3, 4]. Heterogeneities in the overall reduction in transmission and the timing of re-emergence likely reflect differences in NPI patterns, pathogen characteristics, immigration/importation from other countries, and pre-pandemic pathogen dynamics [5]. Therefore, comparing the differential impact of the pandemic perturbations across pathogens can provide unique opportunities to learn about underlying pathogen characteristics, such as their transmissibility or duration of immunity, from heterogeneities in re-emergence patterns [6].

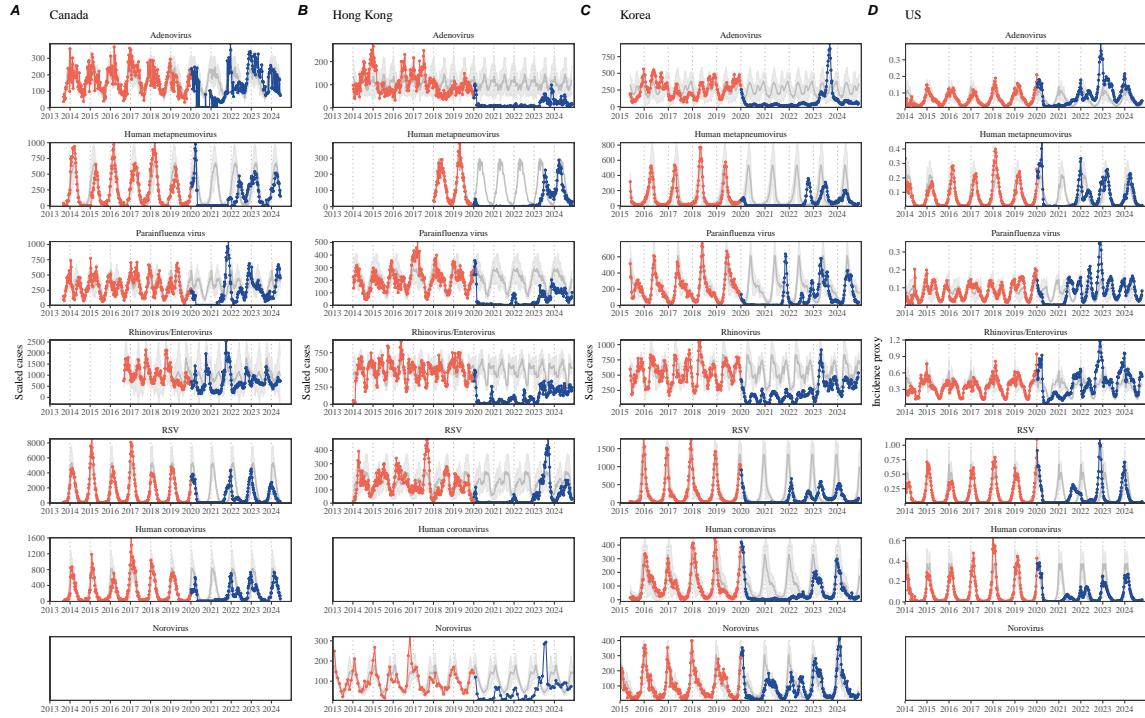


Figure 1: Observed heterogeneity in responses to pandemic perturbations across respiratory pathogens and norovirus in (A) Canada, (B) Hong Kong, (C) Korea, and (D) US. Red points and lines represent data before 2020. Blue points and lines represent data since 2020. Gray lines and shaded regions represent the mean seasonal patterns and corresponding 95% confidence intervals around the mean. Mean seasonal patterns were calculated by aggregating cases before 2020 into 52 weekly bins and taking the average in each week. Cases were scaled to account for changes in testing patterns (Materials and Methods).

Even though more than five years have passed since the emergence of SARS-CoV-2, we still observe persistent changes in pathogen dynamics following the pandemic

36 perturbations: for example, compared to pre-pandemic, seasonal patterns, human
37 metapneumovirus in Korea seem to circulate at lower levels, whereas RSV in Ko-
38 rea seem to exhibit different seasonality (Figure 1). These observations suggest a
39 possibility for a fundamental change in pathogen dynamics following the pandemic
40 perturbations, which can be driven by permanent shift in either human behavior
41 or population-level immunity [7, 8]. The possibility of a long-lasting impact of the
42 pandemic perturbations pose an important question for future infectious disease dy-
43 namics: can we predict whether and when other respiratory pathogens will eventually
44 return to their pre-pandemic dynamics? *[SWP: You suggested: I would say some-
45 thing about the dynamics of these pathogens not being well understood, but I've
46 since rewritten the most of intro and I'm not sure where I would fit this. If you have
47 any suggestions, let me know...]*

48 So far, the majority of epidemiological analyses of respiratory pathogens in the
49 context of the pandemic perturbations have focused on characterizing the timing of
50 rebound [1, 9, 5]. Instead, we seek to characterize how fast a pathogen returns to its
51 pre-pandemic dynamics. These two concepts have subtle but important differences:
52 for example, it took more than 3 years for human metapneumovirus to rebound in
53 Hong Kong but the observed epidemic patterns in 2024 are similar to pre-pandemic
54 seasonal means, suggesting a rapid return to pre-pandemic dynamics following a
55 perturbation (Figure 1). Measuring this rate of return is particularly useful because
56 it allows us to quantify the ecological resilience of a host-pathogen system [10, 11,
57 12, 13].

58 In this study, we lay out theoretical and statistical approaches to characterizing
59 the resilience of a host-pathogen system based on how fast the system recovers from
60 perturbation. We begin by laying out a few representative scenarios that capture
61 the potential impact of pandemic perturbations on endemic pathogen dynamics and
62 illustrate how resilience can be measured by comparing the pre- and post-pandemic
63 dynamics of susceptible and infected hosts. In practice, information on susceptible
64 hosts is often unavailable, making this theoretical approach infeasible. Instead, we
65 utilize a mathematical technique to reconstruct empirical attractors from the data
66 [14], which allows us to measure the rate at which the host-pathogen system ap-
67 proaches this empirical attractor after a perturbation; this rate corresponds to the
68 resilience of the host-pathogen system. We use this method to analyze pathogen
69 surveillance data for respiratory and non-respiratory pathogens from Canada, Hong
70 Kong, Korea, and US. Finally, we show that susceptible host dynamics explain vari-
71 ation in pathogen resilience.

72 Conceptual introduction to pathogen resilience

73 In classical ecological literature, resilience of an ecological system is measured by
74 the rate at which the system returns to its reference state following a perturbation
75 [10, 11, 12, 13]. This rate corresponds to the largest real part of the eigenvalues of

76 the linearized system near equilibrium—here, we refer to this value as the *intrinsic*
77 resilience of the system, which represents the expected rate of return from perturbed
78 states. In practice, we rarely know the true model describing population-level dy-
79 namics of common respiratory pathogens, limiting our ability to infer the intrinsic
80 resilience of a system. Instead, we can still measure the *empirical* resilience of a
81 host-pathogen system by looking at how fast the system returns to the pre-pandemic,
82 endemic dynamics after interventions are lifted.

83 As an example, we begin with a simple Susceptible-Infected-Recovered-Susceptible
84 (SIRS) model with seasonally forced transmission and demography (i.e., birth and
85 death). The SIRS model is the simplest model that allows for waning of immunity
86 and is commonly used for modeling the dynamics of respiratory pathogens [15]. First,
87 consider an intervention that reduce transmission by 50% for 6 months starting in
88 2020, which causes epidemic patterns to deviate from its original stable annual cycle
89 for a short period of time and eventually come back (Figure 2A). To measure the
90 resilience of this system empirically, we first need to be able to measure the dis-
91 tance from its pre-pandemic attractor. There are many ways we can measure the
92 distance from the attractor, but for illustrative purposes, we choose one of the most
93 parsimonious approach: that is, we look at how the susceptible (S) and infected (I)
94 populations change over time and measure the distance on the SI phase plane (Figure
95 2B). In this simple case, the locally estimated scatterplot smoothing (LOESS) fit in-
96 dicates that the distance from the attractor decreases exponentially (linearly on a log
97 scale) on average (Figure 2C). Furthermore, the overall rate of return approximates
98 the intrinsic resilience of the seasonally unforced system (Figure 2C).

99 Alternatively, pandemic perturbations can have a lasting impact on the pathogen
100 dynamics; as an example, we consider a scenario in which a 10% reduction in trans-
101 mission persists even after interevntions are lifted (Figure 2D–F). In such cases in
102 practice, we cannot know whether the pathogen will return to its original cycle or a
103 different cycle until many years have passed, and we cannot measure the distance to
104 the new unknown attractor that the system might eventually approach. Nonethe-
105 less, we can still measure the distance from the pre-pandemic attractor and ask
106 how the distance changes over time (Figure 2E). The LOESS fit suggests that the
107 distance from the pre-pandemic attractor will initially decrease exponentially on av-
108 erage (equivalently, linearly on a log scale) and eventually plateau (Figure 2F). Here,
109 a permanent 10% reduction in transmission rate slows the system, which causes the
110 distance from the pre-pandemic attractor initially to decrease at a slower rate (Figure
111 2F) than it would have otherwise (Figure 2C) before plateauing at a fixed distance
112 between the two attractors. This example shows that resilience is not necessarily an
113 intrinsic property of a specific pathogen. Instead, pathogen resilience is a property
114 of a specific attractor that a host-pathogen system approaches, which depends on
115 both pathogen and host characteristics.

116 Finally, transient phenomena can further complicate the picture (Figure 2G–I).
117 For example, a stage-structured model initially exhibits a stable annual cycle, but
118 perturbations from a 10% reduction in transmission for 6 months cause the epidemic

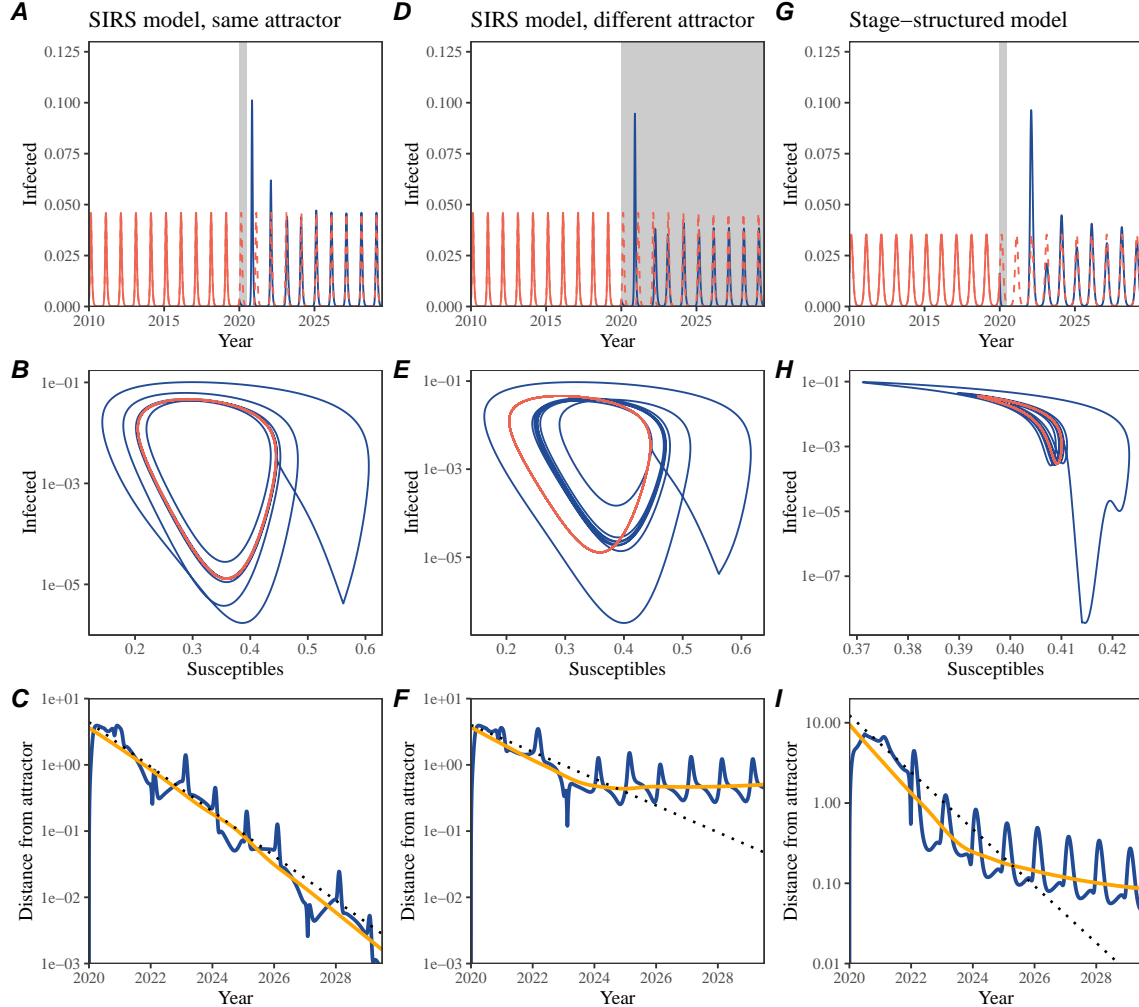


Figure 2: A simple method to measure pathogen resilience following pandemic perturbations across different scenarios. (A, D, G) Simulated epidemic trajectories across various models. Red and blue solid lines represent epidemic dynamics before and after interventions are introduced, respectively. Red dashed lines represent counterfactual epidemic dynamics in the absence of interventions. Gray regions indicate the duration of interventions. (B, E, H) Phase plane representation of the time series in panels A, D, and G alongside the corresponding susceptible host dynamics. Red and blue solid lines represent epidemic trajectories on an SI phase plane before and after interventions are introduced, respectively. (C, F, I) Changes in logged distance from the attractor over time. Blue lines represent the logged distance from the attractor. Orange lines represent the locally estimated scatterplot smoothing (LOESS) fits to the logged distance from the attractor. Dotted lines show the intrinsic resilience of the seasonally unforced system.

to shift to biennial cycles (Figure 2G). The system eventually approaches the original

120 pre-pandemic attractor (Figure 2H), suggesting that this biennial cycle is a transient
121 phenomenon. The LOESS fit indicates that the distance from the attractor initially
122 decreases exponentially at a rate that is consistent with the intrinsic resilience of
123 the seasonally unforced stage-structured system, but the rate of decrease decelerates
124 with the damped oscillations (Figure 2I). This behavior is also referred to as a ghost
125 attractor, which causes long transient dynamics and slow transitions [16]. Strong
126 seasonal forcing in transmission can also lead to transient phenomena for a simple
127 SIRS model, causing a slow return to pre-perturbation dynamics (Supplementary
128 Figure S1).

129 This empirical approach allows us to measure the resilience of a two-strain host-
130 pathogen system even when we have incomplete observation of the infection dynam-
131 ics. Simulations from a simple two-strain system illustrate that separate analyses of
132 individual strain dynamics (e.g., RSV A vs B) and a joint analysis of total infections
133 (e.g., total RSV infections) yield identical resilience estimates (Supplementary Fig-
134 ure S2, 3). This is expected because the dynamics of two strains (or two pathogens)
135 around the attractor in a coupled system are described by the same set of eigen-
136 values and eigenvectors, meaning that both strains should exhibit identical rates of
137 returns following a perturbation. Analogous to a single system, strong seasonal forc-
138 ing in transmission can cause the system to slow down through transient phenomena
139 (Supplementary Figure S4).

140 These observations indicate three possibilities. First, we can directly estimate the
141 empirical resilience of a host-pathogen system by measuring the rate at which the
142 system approaches an attractor, provided that we have a way to quantify the distance
143 from the attractor. The empirical approach to estimating pathogen resilience is
144 particularly convenient because it does not require us to know the true underlying
145 model; estimating the intrinsic resilience from fitting misspecified models can lead
146 to biased estimates (Supplementary Figure S5). Second, resilience estimates allow
147 us to make phenomenological predictions about the dynamics of a host-pathogen
148 system following a perturbation. Assuming that the distance from the attractor will
149 decrease exponentially over time, we can obtain a ballpark estimate for when the
150 system will reach an attractor; this prediction necessarily assumes that there won't
151 be permanent changes in pathogen dynamics (Figure 2F) or a long-term transient
152 phenomenon (Figure 2I). Finally, a change in the rate of an exponential decrease in
153 the distance from the attractor can provide information about whether the system
154 has reached an alternative attractor, or a ghost attractor, that is different from the
155 original, pre-pandemic attractor. These alternative attractors may reflect continued
156 perturbations from permanent changes in transmission patterns as well as changes in
157 immune landscapes. There will be periods of time when it is difficult to tell whether
158 pathogen dynamics are still diverging from its original attractor or have begun to
159 converge to an attractor; now that several years have passed since interventions have
160 been lifted, we expect many respiratory pathogens to have had sufficient time to
161 begin returning to their post-intervention attractors.

162 **Inferring pathogen resilience from real data**

163 Based on these observations, we now lay out our approach to estimating pathogen
164 resilience from real data (Figure 3). We then test this approach against simulations
165 and apply it to real data.

166 So far, we focused on simple examples that assume a constant transmission re-
167 duction. However, in practice, the impact of pandemic perturbations on pathogen
168 transmission is likely more complex (Figure 3A), reflecting introduction and relax-
169 ation of various intervention strategies. In some cases, strong perturbations can even
170 lead to a local fadeout, requiring immigration from another location for epidemic re-
171 emergence. These complexities can lead to longer delays between the introduction of
172 pandemic perturbations and pathogen re-emergence as well as temporal variation in
173 outbreak sizes (Figure 3B): in this example, continued transmission reduction from
174 interventions limits the size of the first outbreak in 2021 following the emergence,
175 allowing for a larger outbreak in 2022 when interventions are further relaxed.

176 Previously, we relied on the dynamics of susceptible and infected hosts to com-
177 pute the distance from the attractor (Figure 2), but information on susceptible hosts
178 is rarely available in practice. In addition, uncertainties in case counts due to obser-
179 vation error as well as multiannual cycles in the observed epidemic dynamics (e.g.,
180 adenovirus circulation patterns in Hong Kong and Korea) add challenges to defin-
181 ing pre-pandemic attractors, which limits our ability to measure the distance from
182 the attractor. To address these challenges, we can reconstruct an empirical attrac-
183 tor by utilizing Takens' theorem [14], which states that an attractor of a nonlinear
184 multidimensional system can be mapped onto a delayed embedding (Materials and
185 Methods). For example, we can use delayed logged values of pre-pandemic cases $C(t)$
186 (Figure 3C) to reconstruct the attractor:

$$\langle \log(C(t) + 1), \log(C(t - \tau) + 1), \dots, \log(C(t - (M - 1)\tau) + 1) \rangle, \quad (1)$$

187 where the delay τ and embedding dimension M are determined based on autocor-
188 relations and false nearest neighbors, respectively [17, 18]. We can then apply the
189 same delay and embedding dimensions to the entire time series to determine the
190 position on a multi-dimensional state space (Figure 3D), which allows us to mea-
191 sure the nearest neighbor distance between the current state of the system and the
192 empirical pre-pandemic attractor (Figure 3E). In theory, we can now quantify how
193 fast this distance decreases by fitting a linear regression on a log scale, where the
194 slope of the linear regression corresponds to pathogen resilience. However, resulting
195 estimates of pathogen resilience can be sensitive to choices about embedding delays
196 and dimensions; for example, using longer delays and higher dimensions tends to
197 smooth out temporal variations in the distance from the attractor (Supplementary
198 Figure S6).

199 Complex changes in the distance from the attractor suggest that estimating
200 pathogen resilience from linear regression will be particularly sensitive to our choice
201 of fitting windows for the regression (Figure 3E). Therefore, before we tried estimat-

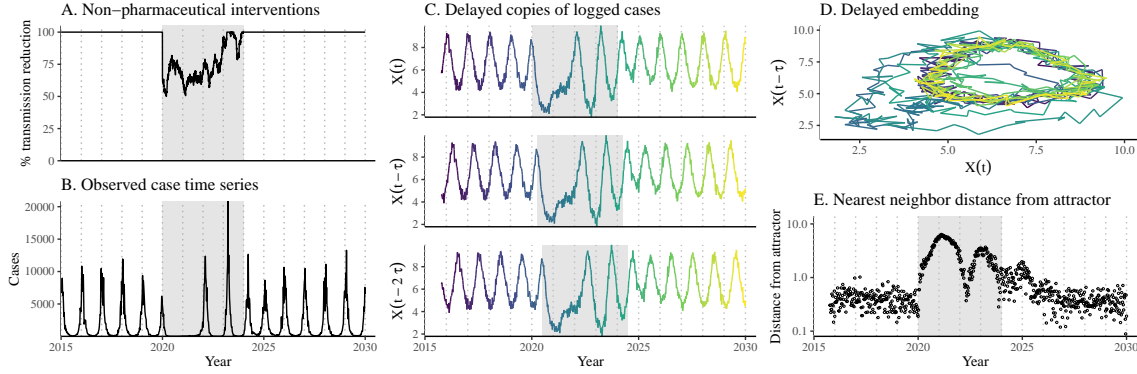


Figure 3: **A schematic diagram explaining the inference of pathogen resilience from synthetic data.** (A) A realistic example of simulated pandemic perturbations, represented by a relative reduction in transmission. (B) The impact of the synthetic pandemic perturbation on epidemic dynamics simulated using a SIRS model with demographic stochasticity. (C) Generating delayed copies of the logged time series allows us to obtain an embedding. (D) Two dimensional representation of an embedding. (E) Delayed embedding allows us to calculate the nearest neighbor distance from the empirical attractor, which is determined based on the pre-pandemic time series. This distance time series can be used to infer pathogen resilience after choosing an appropriate window for linear regression.

ing resilience from real data, we explored an automated window selection criterion for linear regression and test it against randomized, stochastic simulations across a wide range of realistic pandemic perturbation shapes; in doing so, we also explored optimal choices for embedding dimensions and evaluated our choices for fitting window parameters and embedding dimensions by quantifying correlation coefficients between the estimated resilience and the intrinsic resilience of a seasonally unforced system (Materials and Methods). Overall, we find large variation in estimation performances with correlation coefficient ranging from 0.21 to 0.61 (Supplementary Figure S7). In almost all cases, the automated window selection approach outperformed a naive approach that uses the entire time series, starting from the peak distance (Supplementary Figure S7).

Based on the best performing window selection criteria and embedding dimension, we applied this approach to pathogen surveillance data presented in Figure 1 (Materials and Methods). For each time series, we applied Takens' theorem independently to reconstruct the empirical attractor and obtained the corresponding time series of distances from attractors (Supplementary Figure S8). Then, we use the automated window selection criterion to fit a linear regression and estimate the empirical resilience for each pathogen in each country (Supplementary Figure S8); the window selection criterion gave poor regression window for three cases (norovirus in Hong Kong and Korea and Rhinovirus/Enterovirus in the US), leading to unrealistically low resilience estimates, and so we used ad-hoc regression windows instead

223 (Supplementary Figure S9; Materials and Methods).

224 For all pathogens we consider, resilience estimates fall between 0.4/year and
225 1.8/year (Figure 4A). We estimate the mean resilience of common respiratory pathogens
226 to be 0.99/year (95% CI: 0.81/year–1.18/year). As a reference, this is \approx 7.5 times
227 higher than the intrinsic resilience of pre-vaccination measles in England and Wales
228 (\approx 0.13/year). Finally, resilience estimates for norovirus are comparable to those of
229 common respiratory pathogens: 1.44/year (95%CI: 1.01/year–1.87/year) for Hong
230 Kong and 1.07/year (95%CI: 0.86/year–1.29/year) for Korea. Based on a simple
231 ANOVA test, we do not find significant differences in resilience estimates across
232 countries ($p = 0.25$) or pathogens ($p = 0.67$).

233 [SWP: You suggested “I think we probably need to spell out a bit more that
234 long-term changes in the transmission rate (or some other parameter) mean the at-
235 tractor is permanently different and the distance should remain nonzero” and I think
236 we’ve done that enough early on with current revisions so I don’t feel like we need
237 to do it again here. Let me know what you think.] Using resilience estimates, we
238 predicted when each pathogen would hypothetically return to their pre-pandemic
239 dynamics, assuming no long-term change in the attractor. Specifically, we extend
240 our linear regression fits to distance-from-attractor time series and ask when the pre-
241 dicted regression line will cross a threshold value; since we relied on nearest neighbor
242 distances, pre-pandemic distances are always greater than zero (Figure 3E), meaning
243 that we can use the mean of pre-pandemic distances as our threshold.

244 We predict that a return to pre-pandemic cycles would be imminent for most
245 pathogens (Figure 4B). In particular, we predict that 12 out of 23 pathogens should
246 have already returned before the end of 2024. For almost all pathogens that are
247 predicted to have returned already, the observed epidemic dynamics show clear con-
248 vergence towards their pre-pandemic seasonal averages, confirming our predictions
249 (Figure 4C). However, there are a few exceptions, including norovirus in Hong Kong
250 and Rhinovirus/Enterovirus in the US, where the observed epidemic dynamics in
251 2024 exhibit clear deviation from their pre-pandemic seasonal averages (Figure 4C).
252 These observations suggest a possibility that some common respiratory pathogens
253 may have converged to different attractors or are still exhibiting non-equilibrium
254 dynamics. In contrast, pathogens that are predicted to have not returned yet also
255 show clear differences from their pre-pandemic seasonal averages; as many of these
256 pathogens are predicted to return in 2025–2026, we may be able to test these pre-
257 dictions in near future (Supplementary Figure S10). Our reconstructions of distance
258 time series and estimates of pathogen resilience and expected return time are gener-
259 ally robust to choices of embedding dimensions (Supplementary Figure S11–12).

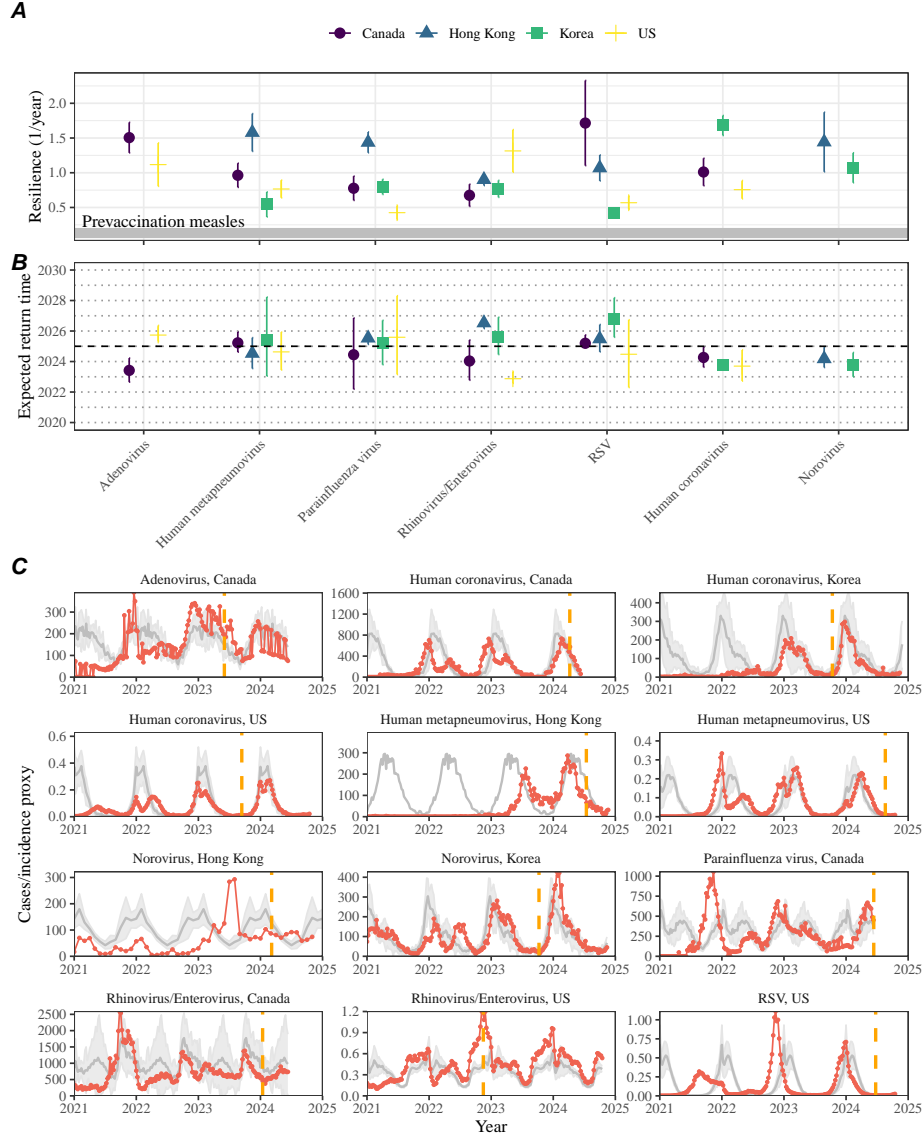


Figure 4: Summary of resilience estimates and predictions for return time. (A) Estimated pathogen resilience. The gray horizontal line represents the intrinsic resilience of pre-vaccination measles dynamics. (B) Predicted timing of when each pathogen will return to their pre-pandemic cycles. The dashed line in panel B indicates the end of 2024 (current observation time). Error bars represent 95% confidence intervals. (C) Observed dynamics for pathogen that are predicted to have returned before the end of 2024. Red points and lines represent data before 2020. Gray lines and shaded regions represent the mean seasonal patterns and corresponding 95% confidence intervals around the mean, previously shown in Figure 1. Orange vertical lines represent the predicted timing of return.

260 **Susceptible host dynamics explain variation in pathogen
261 resilience**

262 So far, we focused on quantifying pathogen resilience from the observed patterns
263 of pathogen re-emergence following pandemic perturbations. But what factors de-
264 termine how resilient a host-pathogen system is? Here, we use the SIRS model to
265 show that susceptible host dynamics are the key determinants of pathogen resilience.
266 To do so, we vary the basic reproduction number \mathcal{R}_0 , which represents the average
267 number of secondary infections caused by a newly infected individual in a fully sus-
268 ceptible population, and the duration of immunity and compute intrinsic resilience
269 for each parameter.

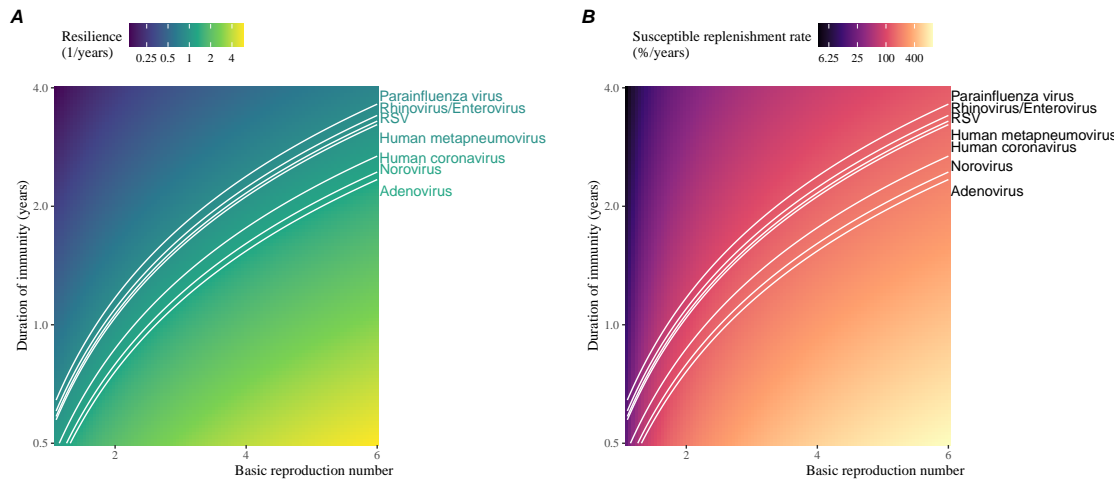


Figure 5: **Linking pathogen resilience to epidemiological parameters and susceptible host dynamics.** (A) The heat map represents intrinsic resilience as a function of the basic reproduction number \mathcal{R}_0 and the duration of immunity. (B) The heat map represents per-capita susceptible replenishment rate as a function of the basic reproduction number \mathcal{R}_0 and the duration of immunity. The standard SIRS model is used to compute intrinsic resilience and per-capita susceptible replenishment rate. Lines correspond to a set of parameters that are consistent with mean resilience estimates for each pathogen. Pathogens are ranked based on their mean resilience estimates, averaged across different countries.

270 We find an increase in \mathcal{R}_0 and a decrease in duration of immunity correspond
271 to an increase in pathogen resilience (Figure 5A). These variations can be under-
272 stood in terms of the susceptible host dynamics, where faster per-capita susceptible
273 replenishment rate causes the system to be more resilient (Figure 5B). This rate can
274 be expressed as a ratio between absolute rate at which new susceptibles enter the
275 population and the equilibrium number of susceptible individuals in the population,
276 \bar{S} . Therefore, both higher \mathcal{R}_0 and shorter duration of immunity can drive faster

277 per-capita susceptible replenishment rate (Figure 5B), especially because higher \mathcal{R}_0
278 leads to lower \bar{S} .

279 We can also rank different pathogens based on the average values of empirical
280 resilience computed previously, which allows us to determine a set of parameters that
281 are consistent with the estimated resilience (Figure 5A). Across all pathogens we
282 consider, except for bocavirus and norovirus, we estimate that the average duration
283 of immunity is likely to be short (< 4 years) across a plausible range of \mathcal{R}_0 (< 6).
284 These rankings further allow us to map each pathogen onto a set of SIRS parameters
285 that are consistent with its empirical resilience (Figure 5A) and obtain a plausible
286 range of susceptible replenishment rates for each pathogen (Figure 5B). However, we
287 note that there is no one-to-one correspondence between susceptible replenishment
288 rates and pathogen resilience, leading to a wide uncertainty in the estimates for
289 susceptible replenishment rates (Figure 5B).

290 **Pathogen resilience determines sensitivity to stochastic perturbations**

291

292 Beyond the pandemic perturbations, we expect host-pathogen systems to experience
293 continued perturbations of varying degrees from changes in epidemiological conditions,
294 such as human behavior, climate, and viral evolution. These perturbations
295 can also arise from demographic stochasticity, which is inherent to any ecological
296 systems. Here, we use a seasonally unforced SIRS model with birth/death to explore
297 how resilience of a host-pathogen system determines the sensitivity to perturbations
298 caused by demographic stochasticity (Materials and Methods).

299 We find that resilience of a host-pathogen system determines the amount of deviation
300 from the deterministic trajectory caused by demographic stochasticity, with less
301 resilient systems experiencing larger deviations (Figure 6). Notably, less resilience
302 systems also exhibit slower epidemic cycles; the periodicity of this epidemic cycle
303 matches those predicted by the intrinsic periodicity of the system (Supplementary
304 Figure S13). These conclusions are robust for the seasonally forced SIRS model
305 (Supplementary Figure S14),

306 **Discussion**

307 The pandemic interventions have caused major disruptions to circulation patterns of
308 both respiratory and non-respiratory pathogens, adding challenges to predicting their
309 future dynamics [1, 2, 3, 4]. However, these perturbations offer large-scale natural
310 experiments for understanding how different pathogens respond to perturbations. In
311 this study, we showed that pathogen re-emergence patterns following pandemic per-
312 turbations can be characterized through the lens of ecological resilience. We showed
313 that variation in pathogen resilience can be explained by the differences in suscepti-

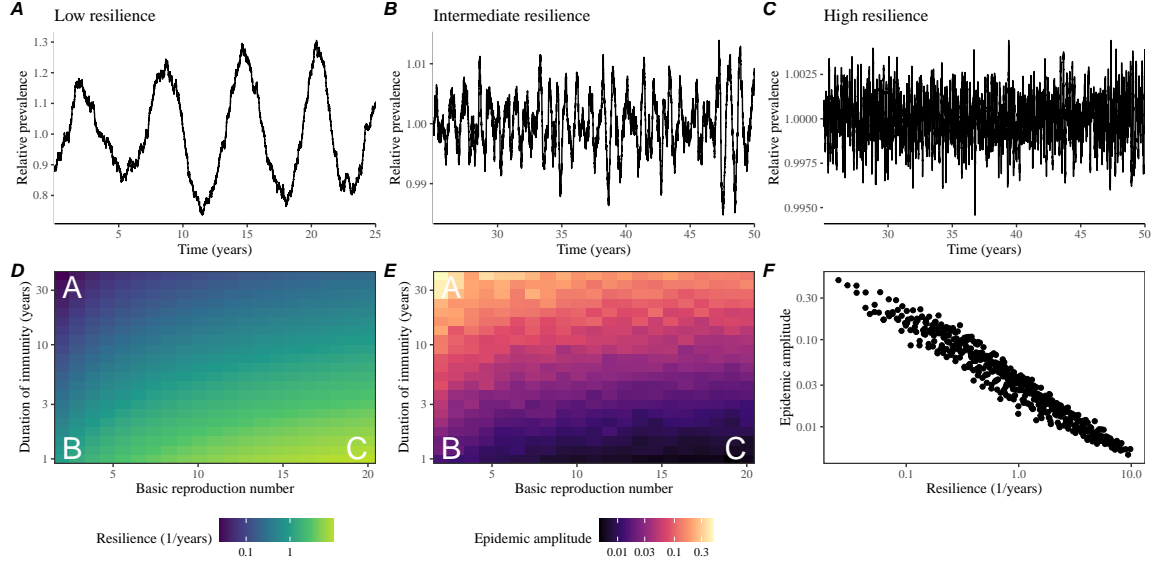


Figure 6: Linking resilience of a host-pathogen system to its sensitivity to stochastic perturbations. (A–C) Epidemic trajectories of a stochastic SIRS model across three different resilience values: low, intermediate, and high. The relative prevalence was calculated by dividing infection prevalence by its mean value. (D) The heat map represents the intrinsic resilience of a system as a function of the basic reproduction number \mathcal{R}_0 and the duration of immunity. (E) The heat map represents the epidemic amplitude as a function of the basic reproduction number \mathcal{R}_0 and the duration of immunity. The epidemic amplitude corresponds to $(\max I - \min I)/(2\bar{I})$, where \bar{I} represents the mean prevalence. (F) The relationship between pathogen resilience and epidemic amplitude.

314 ble host dynamics, where faster replenishment of the susceptible pool corresponds to
 315 a more resilient host-pathogen system. Finally, we showed that pathogen resilience
 316 also determines the sensitivity to stochastic perturbations.

317 We analyzed case time series of common respiratory infections and norovirus
 318 infections from Canada, Hong Kong, Korea, and the US to estimate their resilience.
 319 Overall, we estimated the resilience of these pathogens to range from 0.4/year to
 320 1.8/year, which is 3–14 times more resilient than prevaccination measles. These
 321 resilience estimates indicate that common respiratory pathogens and norovirus likely
 322 exhibit faster susceptible replenishment and are therefore more persistent, indicating
 323 potential challenges in controlling these pathogens.

324 Based on our resilience estimates, we made phenomenological predictions about
 325 when each pathogen will return to their endemic cycles. For the most part, we
 326 accurately predicted which pathogens should have already returned before the end
 327 of 2024. However, there were few exceptions (i.e., norovirus in Hong Kong and
 328 rhinovirus/enterovirus in the US), suggesting a possibility that these may have con-

329 verged to different endemic cycles compared to their pre-pandemic epidemic patterns.
330 These changes may reflect changes in surveillance or actual shift in the dynamics,
331 caused by permanent changes in behavior or population-level immunity. While it may
332 seem unlikely that permanent changes in behavior would only affect a few pathogens
333 and not others, we cannot rule out this possibility given heterogeneity in the age of
334 infection across different respiratory pathogens [19, 20]. Differences in the mode of
335 transmission between respiratory vs gastrointestinal pathogens may also contribute
336 to the differences in responses to pandemic perturbations. However, it is unclear
337 why norovirus dynamics in Korea seemed to have returned, whereas those in Hong
338 Kong have not.

339 For almost half of the pathogens we considered, we predicted that their return
340 to original epidemic patterns is imminent. We will need a few more years of data
341 to test whether these pathogens will eventually return to their original dynamics
342 or eventually converge to a different attractor. Overall, these observations echo
343 earlier studies that highlighted the long-lasting impact of pandemic perturbations
344 [8, 21, 22, 4].

345 We showed that susceptible host dynamics shape pathogen resilience, where faster
346 replenishment of the susceptible population causes the pathogen to be more resilient.
347 For simplicity, we focus on waning immunity and birth as the main drivers of the
348 susceptible host dynamics but other mechanisms can also contribute to the replen-
349 ishment of the susceptible population. In particular, pathogen evolution, especially
350 the emergence of antigenically novel strains, can cause effective waning of immunity
351 in the population; therefore, we hypothesize that faster rates of antigenic evolution
352 can also cause a pathogen to be more resilient. Future studies should explore the
353 relationship between the rate of evolution and resilience for antigenically evolving
354 pathogens.

355 Quantifying pathogen resilience also offers novel approaches to validating population-
356 level epidemiological models. So far, most of model validation in infectious disease
357 ecology is based on the ability of a model to reproduce the observed epidemic dy-
358 namics and to predict future dynamics [23, 24, 25, 26, 27]. However, many models
359 can perform similarly under these criteria. For example, two major RSV models
360 have been proposed to explain biennial epidemic patterns: (1) a stage- and age-
361 structured model that allows disease severity to vary with number of past infections
362 and age of infection [25] and (2) a pathogen-interaction model that accounts for cross
363 immunity between RSV and human metapneumovirus [24]. Since both models can
364 accurately reproduce the observed epidemic patterns, standard criteria for model
365 validation do not allow us to distinguish between these two models from population-
366 level data alone. Instead, it would be possible to measure the empirical resilience of
367 each model by simulating various perturbations and compare them to estimates of
368 empirical resilience from data, using pandemic NPIs as an opportunity.

369 There are several limitations to our work. First, we did not extensively explore
370 other approaches to reconstructing the attractor. Recent studies showed that more
371 sophisticated approaches, such as using non-uniform embedding, can provide more

robust reconstruction for noisy data [18]. In the context of causal inference, choices about embedding can have major impact on the resulting inference [28]. Our resilience estimates are likely overly confident given a lack of uncertainties in attractor reconstruction as well as the simplicity of our statistical framework. Nonetheless, as illustrated in our sensitivity analyses, inferences about pathogen resilience in our SIRS model appear to be robust to decisions about embedding lags and dimensions—this is because tracking the rate at which the system approaches the attractor is likely a much simpler problem than making inferences about causal directionality. Short pre-pandemic time series also limit our ability to accurately reconstruct the attractor and contribute to the crudeness of our resilience estimates; although this is less likely a problem for respiratory pathogens that are strongly annual, our attractor reconstruction may be inaccurate for those exhibiting multi-annual cycles, such as adenovirus in Hong Kong and Korea. Despite these limitations, our qualitative prediction that common respiratory pathogens are more resilient than prevaccination measles is also likely to be robust, given how rapid many respiratory pathogens returned to their original cycles following pandemic NPIs.

Predicting the impact of anthropogenic changes on infectious disease dynamics is a fundamental aim of infectious disease research in a rapidly changing world. Our study illustrates that quantifying pathogen resilience can help us understand how infectious disease pathogens respond to major perturbations caused by NPIs. More broadly, a detailed understanding of the determinants of pathogen resilience may offer unique insights into pathogen persistence and controllability.

Materials and Methods

Data

We gathered time series on respiratory infections from Canada, Hong Kong, Korea, and United States (US). As a reference, we also included time series data on norovirus infections for available countries. In contrast to respiratory pathogens, we expect gastrointestinal viruses, such as norovirus, to be differently affected by pandemic perturbations.

Weekly time series of respiratory infection cases in Canada comes from a publicly available website by the Respiratory Virus Detection Surveillance System, which collect data from select laboratories across Canada [29]. Weekly time series of respiratory infection cases in Hong Kong comes from a publicly available website by the Centre for Health Protection, Department of Health [30, 31]. Weekly time series of acute respiratory infection cases in Korea comes from a publicly available website by the Korea Disease Control and Prevention Agency [32]. Finally, weekly time series of respiratory infection cases in the US were obtained from the National Respiratory and Enteric Virus Surveillance System. Time series on number of tests were also available in Canada, Hong Kong, and the US, but not in Korea. **[SWP: Not sure how to cite NREVSS data because we got it by emailing them...]**

412 **Data processing**

413 For all time series, we rounded every year to 52 weeks by taking the average number
414 of cases and tests between the 52nd and 53rd week. We also rescale all time series to
415 account for changes in testing patterns, which are then used for the actual analysis.

416 For Canada, an increase in testing was observed from 2013 to 2024 (Supplementary
417 Figure S15). To account for this increase, we calculated a 2 year moving average
418 for the number of tests for each pathogen, which we used as a proxy for testing effort.
419 Then, we divided the smoothed testing patterns by the smoothed value at the final
420 week such that the testing effort has a maximum of 1. We then divided weekly cases
421 by the testing effort to obtain a scaled case time series. A similar approach was used
422 earlier for an analysis of RSV time series in the US to account for changes in testing
423 patterns [25].

424 For Hong Kong, we also applied the same scaling procedure to the time series
425 as we did for Canada. In this case, we only adjusted for testing efforts up to the
426 end of 2019 because there was a major reduction in testing for common respiratory
427 pathogens since 2020 (Supplementary Figure S16).

428 For Korea, while we did not have information on testing, the reported number
429 of respiratory infections consistently increased from 2013 to the end of 2019, which
430 we interpreted as changes in testing patterns (Supplementary Figure S17). Since
431 we did not have testing numbers, we used the weekly sum of all acute respiratory
432 viral infection cases as a proxy for testing, which were further smoothed with moving
433 averaged and scaled to have a maximum of 1. For Korea, we also only adjusted for
434 testing efforts up to the end of 2019.

435 In the US, there has been a large increase in testing against some respiratory
436 pathogens, especially RSV, which could not be corrected for through simple scaling
437 (Supplementary Figure S18). Instead, we derived an incidence proxy by multiplying
438 the test positivity with influenza-like illness positivity, which was taken from
439 <https://gis.cdc.gov/grasp/fluview/fluportaldashboard.html>. This method
440 of estimating an incidence proxy has been recently applied in the analysis of seasonal
441 coronaviruses [7] and *Mycoplasma pneumoniae* infections [4]. Detailed assumptions
442 and justifications are provided in [33].

443 **Estimating pathogen resilience**

444 In order to measure pathogen resilience from surveillance data, we first reconstructed
445 the empirical pre-pandemic attractor of the system using Takens' embedding theorem
446 [14]. Specifically, for a given pathogen, we took the pre-pandemic (before 2020)
447 case time series $C(t)$ and reconstruct the attractor using delayed embedding with a
448 uniform delay of τ and dimension M :

$$X_{\tau,m}(t) = \langle \log(C(t) + 1), \log(C(t - \tau) + 1), \dots, \log(C(t - (M - 1)\tau) + 1) \rangle. \quad (2)$$

449 Here, the delay τ was determined by calculating the autocorrelation of the logged
450 pre-pandemic time series and asking when the autocorrelation crosses 0 for the first

451 time [18]; a typical delay for for an annual outbreak is around 13 weeks.

452 Then, for a given delay τ , we determined the embedding dimension M using the
453 false nearest neighbors approach [17, 18]. To do so, we started with an embedding
454 dimension e and construct a set of points $A_{\tau,e} = \{X_{\tau,e}(t) | t < 2020\}$. Then, for
455 each point $X_{\tau,e}(t)$, we determined the nearest neighbor from the set $A_{\tau,e}$, which we
456 denote $X_{\tau,e}(t_{nn})$ for $t \neq t_{nn}$. Then, if the distance between these two points on $e+1$
457 dimension, $D_{\tau,e+1}(t) = \|X_{\tau,e+1}(t_{nn}) - X_{\tau,e+1}(t)\|_2$, is larger than their distance on
458 e dimension, $D_{\tau,e}(t) = \|X_{\tau,e}(t_{nn}) - X_{\tau,e}(t)\|_2$, these two points are deemed to be
459 false nearest neighbors; specifically, we used a threshold R for the ratio between
460 two distances $D_{\tau,e+1}(t)/D_{\tau,e}(t)$ to determine false nearest neighbors. For the main
461 analysis, we used $R = 10$, which was chosen from a sensitivity analysis against
462 simulated data (Supplementary Text). Once we determined the embedding lag τ
463 and dimension M , we apply the embedding to the entire time series and calculate
464 the nearest neighbor distance against the attractor $A_{\tau,M}$ to obtain a time series of
465 distance from the attractor $D_{\tau,M}(t)$.

466 From a time series of distances from the attractor, we estimated pathogen re-
467 silience by fitting a linear regression to an appropriate window. To automatically se-
468 lect the fitting window, we began by smoothing the distance time series using locally
469 estimated scatterplot smoothing (LOESS) to obtain $\hat{D}_{\tau,M}(t)$, where the smoothing
470 is performed on a log scale and exponentiated afterwards. Then, we determined
471 threshold values (T_{start} and T_{end}) for the smoothed distances and choose the fitting
472 window based on when $\hat{D}_{\tau,M}(t)$ crosses these threshold values for the first time.
473 These thresholds were determined by first calculating maximum distance,

$$\max \hat{D} = \max \hat{D}_{\tau,M}(t), \quad (3)$$

474 and mean pre-pandemic distance,

$$\hat{D}_{\text{mean}} = \frac{1}{N_{t<2020}} \sum_{t<2020} \hat{D}_{\tau,M}(t), \quad (4)$$

475 as a reference, and then dividing their ratios into K equal bins:

$$T_{\text{start}} = \hat{D}_{\text{mean}} \times \left(\frac{\max \hat{D}}{\hat{D}_{\text{mean}}} \right)^{(K-a)/K} \quad (5)$$

$$T_{\text{end}} = \hat{D}_{\text{mean}} \times \left(\frac{\max \hat{D}}{\hat{D}_{\text{mean}}} \right)^{a/K} \quad (6)$$

476 where a represents the truncation threshold. This allows us to discard the initial
477 period during which the distance increases (from the introduction of intervention
478 measures) and the final period during which the distance plateaus (as the system
479 reaches an attractor). The fitting window is determined based on when the smoothed
480 distance $\hat{D}_{\tau,M}(t)$ crosses these threshold values for the first time; then, we fit a

481 linear regression to logged (unsmoothed) distances $\log D_{\tau,M}(t)$ using that window.
 482 Alongside the threshold R for the false nearest neighbors approach, we tested optimal
 483 choices for K and a values using simulations (Supplementary Text). We used $K = 19$
 484 and $a = 2$ throughout the paper based on the simulation results.

485 Mathematical modeling

486 Throughout the paper, we use a series of mathematical models to illustrate the
 487 concept of pathogen resilience and to understand the determinants of pathogen re-
 488 silience. In general, the intrinsic resilience for a given system is given by the largest
 489 real part of the eigenvalues of the linearized system at endemic equilibrium. Here, we
 490 focus on the SIRS model with demography (birth and death) and present the details
 491 of other models in Supplementary Text. The SIRS (Susceptible-Infected-Recovered-
 492 Susceptible) model is the simplest model that allows for waning of immunity, where
 493 recovered (immune) individuals are assumed to become fully susceptible after an
 494 average of $1/\delta$ time period. The dynamics of the SIRS model is described by the
 495 following set of differential equations:

$$\frac{dS}{dt} = \mu - \beta(t)SI - \mu S + \delta R \quad (7)$$

$$\frac{dI}{dt} = \beta(t)SI - (\gamma + \mu)I \quad (8)$$

$$\frac{dR}{dt} = \gamma I - (\delta + \mu)R \quad (9)$$

(10)

496 where μ represents the birth/death rate, $\beta(t)$ represents the time-varying trans-
 497 mission rate, and γ represents the recovery rate. The basic reproduction number
 498 $\mathcal{R}_0(t) = \beta(t)/(\gamma + \mu)$ is defined as the average number of secondary infections that
 499 a single infected individual would cause in a fully susceptible population at time t
 500 and measures the intrinsic transmissibility of a pathogen.

501 When we first introduced the idea of pathogen resilience (Figure 2), we imposed
 502 sinusoidal changes to the transmission rate to account for seasonal transmission:

$$\beta(t) = b_1(1 + \theta \cos(2\pi(t - \phi)))\alpha(t), \quad (11)$$

503 where b_1 represents the baseline transmission rate, θ represents the seasonal ampli-
 504 tude, and ϕ represents the seasonal offset term. Here, we also introduced an extra
 505 multiplicative term $\alpha(t)$ to account for the impact of pandemic perturbations, where
 506 $\alpha(t) < 1$ indicates transmission reduction. Figure 2A and 2B were generated assum-
 507 ing $b_1 = 3 \times (365/7 + 1/50)/\text{years}$, $\theta = 0.2$, $\phi = 0$, $\mu = 1/50/\text{years}$, $\gamma = 365/7/\text{years}$,
 508 and $\delta = 1/2/\text{years}$. In Figure 2A, we imposed a 50% transmission reduction for 6
 509 months from 2020:

$$\alpha(t) = \begin{cases} 0.5 & 2020 \leq t < 2020.5 \\ 1 & \text{otherwise} \end{cases} \quad (12)$$

510 In Figure 2B, we imposed a 50% transmission reduction for 6 months from 2020 and
 511 a permanent 10% reduction onward:

$$\alpha(t) = \begin{cases} 1 & t < 2020 \\ 0.5 & 2020 \leq t < 2020.5 \\ 0.9 & 2020.5 \leq t \end{cases} \quad (13)$$

512 In both scenarios, we simulated the SIRS model from the following initial conditions
 513 ($S(0) = 1/\mathcal{R}_0$, $I(0) = 1 \times 10^{-6}$, and $R(0) = 1 - S(0) - I(0)$) from 1900 until 2030.

514 To measure the empirical resilience of the SIRS model (Figure 2C and 2F), we
 515 computed the normalized distance between post-intervention susceptible and logged
 516 infected proportions and their corresponding unperturbed values at the same time:

$$\sqrt{\left(\frac{S(t) - S_{\text{unperturbed}}(t)}{\sigma_S}\right)^2 + \left(\frac{\log I(t) - \log I_{\text{unperturbed}}(t)}{\sigma_{\log I}}\right)^2}, \quad (14)$$

517 where σ_S and $\sigma_{\log I}$ represent the standard deviation in the unperturbed susceptible
 518 and logged infected proportions. The unperturbed values were obtained by simulating
 519 the same SIRS model without pandemic perturbations ($\alpha = 1$). We normalized
 520 the differences in susceptible and logged infected proportions to allow both quantities
 521 to equally contribute to the changes in distance from the attractor. We used logged
 522 prevalence, instead of absolute prevalence, in order to capture epidemic dynamics
 523 in deep troughs during the intervention period. In Supplementary Materials, we
 524 also compared how the degree of seasonal transmission affects empirical resilience
 525 by varying θ from 0 to 0.4; when we assumed no seasonality ($\theta = 0$), we did not
 526 normalize the distance because the standard deviation of pre-intervention dynamics
 527 are zero.

528 We used the SIRS model to understand how underlying epidemiological parameters
 529 affect pathogen resilience and link this relationship to underlying susceptible
 530 host dynamics. For the simple SIRS model without seasonal transmission ($\theta = 0$),
 531 the intrinsic resilience corresponds to

$$-\frac{\text{Re}(\lambda)}{2} = \frac{\delta + \beta I^* + \mu}{2}. \quad (15)$$

532 Here, I^* represents the prevalence at endemic equilibrium:

$$I^* = \frac{(\delta + \mu)(\beta - (\gamma + \mu))}{\beta(\delta + \gamma + \mu)}. \quad (16)$$

533 The susceptible replenishment rate is given by

$$S_{\text{replenish}} = \frac{\mu + \delta R}{S^*}, \quad (17)$$

534 where $S^* = 1/\mathcal{R}_0$ represents the equilibrium proportion of susceptible individuals.
 535 We varied the basic reproduction number \mathcal{R}_0 between 1.1 to 6 and the average

duration of immunity $1/\delta$ between 2 to 4 years, and computed these two quantities.
In doing so, we fixed all other parameters: $\mu = 1/80/\text{years}$ and $\gamma = 365/7/\text{years}$.

Finally, we used a seasonally unforced stochastic SIRS model without demography to understand how pathogen resilience affects sensitivity of the system to demographic stochasticity (see Supplementary Text for the details of the stochastic SIRS model). By varying the basic reproduction number \mathcal{R}_0 between 2 to 20 and the average duration of immunity $1/\delta$ between 1 to 40 years, we ran the the SIRS model for 100 years and computed the epidemic amplitude, which we defined as $(\max I - \min I)/(2\bar{I})$. Each simulation began from the equilibrium, and we truncated initial 25 years before computing the epidemic amplitude. In doing so, we assumed $\gamma = 365/7/\text{years}$ and fixed the population size to 1 billion to prevent any fadeouts. We also considered using a seasonally forced stochastic SIRS model without demography, assuming an amplitude of seasonal forcing of 0.04; in this case, we computed the relative epidemic amplitude by comparing the deterministic and stochastic trajectories (Supplementary Materials).

551 Data availability

552 All data and code are stored in a publicly available GitHub repository (<https://github.com/cobeylab/return-time>).
553

554 Funding

555 S.W.P. is a Peter and Carmen Lucia Buck Foundation Awardee of the Life Sciences
556 Research Foundation.

557 **Supplementary Text**

558 **Resilience of a stage-structured system.**

559 In Figure 2G–I, we used a more realistic, stage-structured model to illustrate how
 560 transient phenomena can cause the system to slow down. Specifically, we used the
 561 stage-structured RSV model proposed by [25], which assumes that subsequent rein-
 562 fections cause an individual to become less susceptible and transmissible than previ-
 563 ous infections. The model dynamics can be described as follows:

$$\frac{dM}{dt} = \mu - (\omega + \mu)M \quad (S1)$$

$$\frac{dS_0}{dt} = \omega M - (\lambda(t) + \mu)S_0 \quad (S2)$$

$$\frac{dI_1}{dt} = \lambda(t)S_0 - (\gamma_1 + \mu)I_1 \quad (S3)$$

$$\frac{dS_1}{dt} = \gamma_1 I_1 - (\sigma_1 \lambda(t) + \mu)S_1 \quad (S4)$$

$$\frac{dI_2}{dt} = \sigma_1 \lambda(t)S_1 - (\gamma_2 + \mu)I_2 \quad (S5)$$

$$\frac{dS_2}{dt} = \gamma_2 I_2 - (\sigma_2 \lambda(t) + \mu)S_2 \quad (S6)$$

$$\frac{dI_3}{dt} = \sigma_2 \lambda(t)S_2 - (\gamma_3 + \mu)I_3 \quad (S7)$$

$$\frac{dS_3}{dt} = \gamma_3 I_3 - (\sigma_3 \lambda(t) + \mu)S_3 + \gamma_4 I_4 \quad (S8)$$

$$\frac{dI_4}{dt} = \sigma_3 \lambda(t)S_3 - (\gamma_4 + \mu)I_4 \quad (S9)$$

(S10)

564 where M represents the proportion of individuals who are maternally immune; S_i
 565 represents the proportion of individuals who are susceptible after i prior infections; I_i
 566 represents the proportion of individuals who are currently (re)-infected with their i -th
 567 infection; μ represents the birth and death rates; $1/\omega$ represents the mean duration
 568 of maternal immunity; $1/\gamma_i$ represents the mean duration of infection; $\lambda(t)$ represents
 569 the force of infection; and σ_i represents the reduction in susceptibility for the i -th
 570 reinfection. The force of infection is modeled using a sinusoidal function:

$$\beta(t) = b_1(1 + \theta \cos(2\pi(t - \phi)))\alpha(t) \quad (S11)$$

$$\lambda(t) = \beta(I_1 + \rho_1 I_2 + \rho_2(I_3 + I_4)), \quad (S12)$$

571 where b_1 represents the baseline transmission rate; θ represents the seasonal ampli-
 572 tude; ϕ represents the seasonal offset term; $\alpha(t)$ represents the intervention effect;
 573 and ρ_i represents the impact of immunity on transmission reduction. We used the

574 following parameters to simulate the impact of interventions on epidemic dynam-
 575 ics [25]: $b_1 = 9 \times (365/10 + 1/80)/\text{years}$, $\theta = 0.2$, $\phi = -0.1$, $\omega = 365/112/\text{years}$,
 576 $\gamma_1 = 365/10/\text{years}$, $\gamma_2 = 365/7/\text{years}$, $\gamma_3 = 365/5/\text{years}$, $\sigma_1 = 0.76$, $\sigma_2 = 0.6$,
 577 $\sigma_3 = 0.4$, $\rho_1 = 0.75$, $\rho_2 = 0.51$, and $\mu = 1/80/\text{years}$. We assumed a 50% transmis-
 578 sion reduction for 6 months from 2020:

$$\alpha(t) = \begin{cases} 0.5 & 2020 \leq t < 2020.5 \\ 1 & \text{otherwise} \end{cases} \quad (\text{S13})$$

579 The model was simulated from 1900 to 2030 using the following initial conditions:
 580 $M = 0$, $S_0 = 1/\mathcal{R}_0 - I_1$, $I_1 = 1 \times 10^{-6}$, $S_1 = 1 - 1/\mathcal{R}_0$, $I_2 = 0$, $S_2 = 0$, $I_3 = 0$,
 581 $S_3 = 0$, and $I_4 = 0$. For the phase plane analysis (Figure 2H) and distance analysis
 582 (Figure 2I), we relied on the average susceptibility,

$$\bar{S} = S_0 + \sigma_1 S_1 + \sigma_2 S_2 + \sigma_3 S_3, \quad (\text{S14})$$

583 and total prevalence,

$$I_{\text{total}} = I_1 + I_2 + I_3 + I_4. \quad (\text{S15})$$

584 These quantities were used to compute the normalized distance from the attractor,
 585 as described in the main text.

586 Resilience of a multistrain system.

587 We used a simple two-strain model to show that a multistrain host-pathogen system
 588 that is coupled through cross immunity can be described by a single resilience value.
 589 The model dynamics can be described as follows [24]:

$$\frac{dS}{dt} = \mu - \mu S - (\lambda_1 + \lambda_2)S + \rho_1 R_1 + \rho_2 R_2 \quad (\text{S16})$$

$$\frac{dI_1}{dt} = \lambda_1 S - (\gamma_1 + \mu)I_1 \quad (\text{S17})$$

$$\frac{dI_2}{dt} = \lambda_2 S - (\gamma_2 + \mu)I_2 \quad (\text{S18})$$

$$\frac{dR_1}{dt} = \gamma_1 I_1 - \lambda_2 \epsilon_{21} R_1 - \rho_1 R_1 + \rho_2 R - \mu R_1 \quad (\text{S19})$$

$$\frac{dR_2}{dt} = \gamma_2 I_2 - \lambda_1 \epsilon_{12} R_2 - \rho_2 R_2 + \rho_1 R - \mu R_2 \quad (\text{S20})$$

$$\frac{dJ_1}{dt} = \lambda_1 \epsilon_{12} R_2 - (\gamma_1 + \mu)J_1 \quad (\text{S21})$$

$$\frac{dJ_2}{dt} = \lambda_2 \epsilon_{21} R_1 - (\gamma_2 + \mu)J_2 \quad (\text{S22})$$

$$\frac{dR}{dt} = \gamma_1 J_1 + \gamma_2 J_2 - \rho_1 R - \rho_2 R - \mu R \quad (\text{S23})$$

where S represents the proportion of individuals who are fully susceptible to infections by both strains; I_1 represents the proportion of individuals who are infected with strain 1 without prior immunity; I_2 represents the proportion of individuals who are infected with strain 2 without prior immunity; R_1 represents the proportion of individuals who are fully immune against strain 1 and partially susceptible to reinfection by strain 2; R_2 represents the proportion of individuals who are fully immune against strain 2 and partially susceptible to reinfection by strain 1; J_1 represents the proportion of individuals who are infected with strain 1 with prior immunity against strain 2; J_2 represents the proportion of individuals who are infected with strain 2 with prior immunity against strain 1; R represents the proportion of individuals who are immune to infections from both strains; μ represents the birth/death rate; λ_1 and λ_2 represent the force of infection from strains 1 and 2, respectively; ρ_1 and ρ_2 represent the waning immunity rate; γ_1 and γ_2 represent the recovery rate; ϵ_{12} and ϵ_{21} represent the susceptibility to reinfection with strains 2 and 1, respectively, given prior immunity from infection with strains 1 and 2, respectively. The force of infection is modeled as follows:

$$\beta_1 = b_1(1 + \theta_1 \sin(2\pi(t - \phi_1)))\alpha(t) \quad (\text{S24})$$

$$\beta_2 = b_2(1 + \theta_2 \sin(2\pi(t - \phi_2)))\alpha(t) \quad (\text{S25})$$

$$\lambda_1 = \beta_1(I_1 + J_1) \quad (\text{S26})$$

$$\lambda_2 = \beta_2(I_2 + J_2) \quad (\text{S27})$$

In Supplementary Figures S2–S4, we assumed the following parameters: $b_1 = 2 \times 52/\text{years}$, $b_2 = 4 \times 52/\text{years}$, $\phi_1 = \phi_2 = 0$, $\epsilon_{12} = 0.9$, $\epsilon_{21} = 0.5$, $\gamma_1 = \gamma_2 = 52/\text{years}$, $\rho_1 = \rho_2 = 1/\text{years}$, and $\mu = 1/70/\text{years}$. For all simulations, we assumed a 50% transmission reduction for 6 months from 2020:

$$\alpha(t) = \begin{cases} 0.5 & 2020 \leq t < 2020.5 \\ 1 & \text{otherwise} \end{cases} \quad (\text{S28})$$

The seasonal amplitude θ is varied from 0 to 0.4. All simulations were ran from 1900 to 2030 with following initial conditions: $S(0) = 1 - 2 \times 10^{-6}$, $I_1(0) = 1 \times 10^{-6}$, $I_2(0) = 1 \times 10^{-6}$, $R_1(0) = 0$, $R_2(0) = 0$, $J_1(0) = 0$, $J_2(0) = 0$, and $R(0) = 0$.

We considered three scenarios for measuring pathogen resilience: (1) we only have information about strain 1, (2) we only have information about strain 2, and (3) we are unable to distinguish between strains. In the first two scenarios (see panels A–C for strain 1 and panels D–F for strain 2), we considered the dynamics of average susceptibility for each strain and total prevalence:

$$\bar{S}_1 = S + \epsilon_{12}R_2 \quad (\text{S29})$$

$$\hat{I}_1 = I_1 + J_1 \quad (\text{S30})$$

$$\bar{S}_2 = S + \epsilon_{21}R_1 \quad (\text{S31})$$

$$\hat{I}_2 = I_2 + J_2 \quad (\text{S32})$$

618 In the third scenario (panels G–I), we considered the dynamics of total susceptible
 619 and infected populations:

$$\hat{S} = S + R_2 + R_1 \quad (\text{S33})$$

$$\hat{I} = I_1 + J_1 + I_2 + J_2 \quad (\text{S34})$$

620 These quantities were used to compute the normalized distance from the attractor,
 621 as described in the main text.

622 Estimating intrinsic resilience using mechanistic model

623 We tested whether we can reliably estimate the intrinsic resilience of a system by fit-
 624 ting a mechanistic model. Specifically, we simulated case time series from stochastic
 625 SIRS and two-strain models and fitted a simple, deterministic SIRS model using a
 626 Bayesian framework.

627 We simulated the models in discrete time with a daily time step ($\Delta t = 1$),
 628 incorporating demographic stochasticity:

$$\beta(t) = \mathcal{R}_0 \left(1 + \theta \cos \left(\frac{2\pi t}{364} \right) \right) \alpha(t)(1 - \exp(-\gamma)) \quad (\text{S35})$$

$$\text{FOI}(t) = \beta(t)I(t - \Delta t)/N \quad (\text{S36})$$

$$B(t) \sim \text{Poisson}(\mu N) \quad (\text{S37})$$

$$\Delta S(t) \sim \text{Binom}(S(t - \Delta t), 1 - \exp(-(\text{FOI}(t) + \mu)\Delta t)) \quad (\text{S38})$$

$$N_{SI}(t) \sim \text{Binom}\left(\Delta S(t), \frac{\text{FOI}(t)}{\text{FOI}(t) + \mu}\right) \quad (\text{S39})$$

$$\Delta I(t) \sim \text{Binom}(I(t - \Delta t), 1 - \exp(-(\gamma + \mu)\Delta t)) \quad (\text{S40})$$

$$N_{IR}(t) \sim \text{Binom}\left(\Delta I(t), \frac{\gamma}{\gamma + \mu}\right) \quad (\text{S41})$$

$$\Delta R(t) \sim \text{Binom}(R(t - \Delta t), 1 - \exp(-(\delta + \mu)\Delta t)) \quad (\text{S42})$$

$$N_{RS}(t) \sim \text{Binom}\left(\Delta R(t), \frac{\delta}{\delta + \mu}\right) \quad (\text{S43})$$

$$S(t) = S(t - \Delta t) + N_{RS}(t) + B(t) - \Delta S(t) \quad (\text{S44})$$

$$I(t) = I(t - \Delta t) + N_{SI}(t) - \Delta I(t) \quad (\text{S45})$$

$$R(t) = R(t - \Delta t) + N_{IR}(t) - \Delta R(t) \quad (\text{S46})$$

629 where FOI represent the force of infection; N_{ij} represent the number of individuals
 630 moving from compartment i to j on a given day; and $B(t)$ represents the number
 631 of new births. We simulated the model on a daily scale—assuming 364 days in a
 632 year so that it can be evenly grouped into 52 weeks—with the following parameters:
 633 $\mathcal{R}_0 = 3$, $\theta = 0.1$, $\gamma = 1/7/\text{days}$, $\delta = 1/(364 \times 2)/\text{days}$, $\mu = 1/(364 \times 50)/\text{days}$, and
 634 $N = 1 \times 10^8$. The model was simulated from 1900 to 2030 assuming $S(0) = N/3$,

⁶³⁵ $I(0) = 100$, and $R(0) = N - S(0) - I(0)$. The observed incidence from the model
⁶³⁶ was then simulated as follows:

$$C(t) = \text{Beta-Binom}(N_{SI}(t), \rho, k), \quad (\text{S47})$$

⁶³⁷ where ρ represents the reporting probability and k represents the overdispersion
⁶³⁸ parameter of beta-binomial distribution. Here, we used the beta-binomial distribu-
⁶³⁹ tion to account for overdispersion in reporting. We assumed $\rho = 0.002$ (i.e., 0.2%
⁶⁴⁰ probability) and $k = 1000$.

⁶⁴¹ We used an analogous approach for the two-strain model:

$$\beta_1(t) = b_1 \left(1 + \theta_1 \cos \left(\frac{2\pi(t - \phi_1)}{364} \right) \right) \alpha(t) \quad (\text{S48})$$

$$\beta_2(t) = b_2 \left(1 + \theta_2 \cos \left(\frac{2\pi(t - \phi_2)}{364} \right) \right) \alpha(t) \quad (\text{S49})$$

$$\text{FOI}_1(t) = \beta_1(t)(I_1(t - \Delta t) + J_1(t - \Delta t))/N \quad (\text{S50})$$

$$\text{FOI}_2(t) = \beta_2(t)(I_2(t - \Delta t) + J_2(t - \Delta t))/N \quad (\text{S51})$$

$$B(t) \sim \text{Poisson}(\mu N) \quad (\text{S52})$$

$$\Delta S(t) \sim \text{Binom}(S(t - \Delta t), 1 - \exp(-(\text{FOI}_1(t) + \text{FOI}_2(t) + \mu)\Delta t)) \quad (\text{S53})$$

$$N_{SI_1}(t) \sim \text{Binom}\left(\Delta S(t), \frac{\text{FOI}_1(t)}{\text{FOI}_1(t) + \text{FOI}_2(t) + \mu}\right) \quad (\text{S54})$$

$$N_{SI_2}(t) \sim \text{Binom}\left(\Delta S(t), \frac{\text{FOI}_2(t)}{\text{FOI}_1(t) + \text{FOI}_2(t) + \mu}\right) \quad (\text{S55})$$

$$\Delta I_1(t) \sim \text{Binom}(I_1(t - \Delta t), 1 - \exp(-(\gamma_1 + \mu)\Delta t)) \quad (\text{S56})$$

$$N_{I_1 R_1}(t) \sim \text{Binom}\left(\Delta I_1(t), \frac{\gamma_1}{\gamma_1 + \mu}\right) \quad (\text{S57})$$

$$\Delta I_2(t) \sim \text{Binom}(I_2(t - \Delta t), 1 - \exp(-(\gamma_2 + \mu)\Delta t)) \quad (\text{S58})$$

$$N_{I_2 R_2}(t) \sim \text{Binom}\left(\Delta I_2(t), \frac{\gamma_2}{\gamma_2 + \mu}\right) \quad (\text{S59})$$

$$\Delta R_1(t) \sim \text{Binom}(R_1(t - \Delta t), 1 - \exp(-(\epsilon_{21}\text{FOI}_2(t) + \rho_1 + \mu)\Delta t)) \quad (\text{S60})$$

$$N_{R_1 S}(t) \sim \text{Binom}\left(\Delta R_1(t), \frac{\rho_1}{\epsilon_{21}\text{FOI}_2(t) + \rho_1 + \mu}\right) \quad (\text{S61})$$

$$N_{R_1 J_2}(t) \sim \text{Binom}\left(\Delta R_1(t), \frac{\epsilon_{21}\text{FOI}_2(t)}{\epsilon_{21}\text{FOI}_2(t) + \rho_1 + \mu}\right) \quad (\text{S62})$$

$$\Delta R_2(t) \sim \text{Binom}(R_2(t - \Delta t), 1 - \exp(-(\epsilon_{12}\text{FOI}_1(t) + \rho_2 + \mu)\Delta t)) \quad (\text{S63})$$

$$N_{R_2 S}(t) \sim \text{Binom}\left(\Delta R_2(t), \frac{\rho_2}{\epsilon_{12}\text{FOI}_1(t) + \rho_2 + \mu}\right) \quad (\text{S64})$$

$$N_{R_2 J_1}(t) \sim \text{Binom}\left(\Delta R_2(t), \frac{\epsilon_{12}\text{FOI}_1(t)}{\epsilon_{12}\text{FOI}_1(t) + \rho_2 + \mu}\right) \quad (\text{S65})$$

$$\Delta J_1(t) \sim \text{Binom}(J_1(t - \Delta t), 1 - \exp(-(\gamma_1 + \mu)\Delta t)) \quad (\text{S66})$$

$$N_{J_1R}(t) \sim \text{Binom}\left(\Delta J_1(t), \frac{\gamma_1}{\gamma_1 + \mu}\right) \quad (\text{S67})$$

$$\Delta J_2(t) \sim \text{Binom}(J_2(t - \Delta t), 1 - \exp(-(\gamma_2 + \mu)\Delta t)) \quad (\text{S68})$$

$$N_{J_2R}(t) \sim \text{Binom}\left(\Delta J_2(t), \frac{\gamma_2}{\gamma_2 + \mu}\right) \quad (\text{S69})$$

$$\Delta R(t) \sim \text{Binom}(R(t - \Delta t), 1 - \exp(-(\rho_1 + \rho_2 + \mu)\Delta t)) \quad (\text{S70})$$

$$N_{RR_1}(t) \sim \text{Binom}\left(\Delta R(t), \frac{\rho_1}{\rho_1 + \rho_2 + \mu}\right) \quad (\text{S71})$$

$$N_{RR_2}(t) \sim \text{Binom}\left(\Delta R(t), \frac{\rho_2}{\rho_1 + \rho_2 + \mu}\right) \quad (\text{S72})$$

$$S(t) = S(t - \Delta t) - \Delta S(t) + B(t) + N_{R_1S}(t) + N_{R_2S}(t) \quad (\text{S73})$$

$$I_1(t) = I_1(t - \Delta t) - \Delta I_1(t) + N_{SI_1}(t) \quad (\text{S74})$$

$$I_2(t) = I_2(t - \Delta t) - \Delta I_2(t) + N_{SI_2}(t) \quad (\text{S75})$$

$$R_1(t) = R_1(t - \Delta t) - \Delta R_1(t) + N_{I_1R_1}(t) + N_{RR_1}(t) \quad (\text{S76})$$

$$R_2(t) = R_2(t - \Delta t) - \Delta R_2(t) + N_{I_2R_2}(t) + N_{RR_2}(t) \quad (\text{S77})$$

$$J_1(t) = J_1(t - \Delta t) - \Delta J_1(t) + N_{R_2J_1}(t) \quad (\text{S78})$$

$$J_2(t) = J_2(t - \Delta t) - \Delta J_2(t) + N_{R_1J_2}(t) \quad (\text{S79})$$

$$R(t) = R(t - \Delta t) - \Delta R(t) + N_{J_1R}(t) + N_{J_2R}(t) \quad (\text{S80})$$

We simulated the model on a daily scale with previously estimated parameters for the RSV-HMPV interaction [24]: $b_1 = 1.7/\text{weeks}$, $b_2 = 1.95/\text{weeks}$, $\theta_1 = 0.4$, $\theta_2 = 0.3$, $\phi_1 = 0.005 \times 7/364$, $\phi_2 = 4.99 \times 7/364$, $\epsilon_{12} = 0.92$, $\epsilon_{21} = 0.45$, $\gamma_1 = 1/10/\text{days}$, $\gamma_2 = 1/10/\text{days}$, $\rho_1 = 1/364/\text{days}$, $\rho_2 = 1/364/\text{days}$, $\mu = 1/(70 \times 364)/\text{days}$, and $N = 1 \times 10^8$. The model was simulated from 1900 to 2030 assuming $S(0) = N - 200$, $I_1(0) = 100$, $I_2(0) = 100$, $R_1(0) = 0$, $R_2(0) = 0$, $J_1(0) = 0$, $J_2(0) = 0$, and $R(0) = 0$. The observed incidence for each strain is then simulated as follows:

$$C_1(t) = \text{Beta-Binom}(N_{SI_1}(t) + N_{R_2J_1}, \rho, k), \quad (\text{S81})$$

$$C_2(t) = \text{Beta-Binom}(N_{SI_2}(t) + N_{R_1J_2}, \rho, k), \quad (\text{S82})$$

where ρ represents the reporting probability and k represents the overdispersion parameter of beta-binomial distribution. We assumed $\rho = 0.002$ (i.e., 0.2% probability) and $k = 500$. We also considered the total incidence: $C_{\text{total}}(t) = C_1(t) + C_2(t)$.

For both models, we considered a more realistically shaped pandemic perturbation $\alpha(t)$ to challenge our ability to estimate the intervention effects. Thus, we assumed a 40% transmission reduction for 3 months from March 2020, followed by a 10% transmission reduction for 6 months, 20% transmission reduction for 3 months,

656 and a final return to normal levels:

$$\alpha(t) = \begin{cases} 1 & t < 2020.25 \\ 0.6 & 2020.25 \leq t < 2020.5 \\ 0.9 & 2020.5 \leq t < 2021 \\ 0.8 & 2021 \leq t < 2021.25 \\ 1 & 2021.25 \leq t \end{cases}. \quad (\text{S83})$$

657 For all simulations, we truncated the time series from the beginning of 2014 to the
658 end of 2023 and aggregate them into weekly cases.

659 To infer intrinsic resilience from time series, we fitted a simple discrete time,
660 deterministic SIRS model [4]:

$$\Delta t = 1 \text{ week} \quad (\text{S84})$$

$$\text{FOI}(t) = \beta(t)(I(t - \Delta t) + \omega)/N \quad (\text{S85})$$

$$\Delta S(t) = [1 - \exp(-(\text{FOI}(t) + \mu)\Delta t)] S(t - \Delta t) \quad (\text{S86})$$

$$N_{SI}(t) = \frac{\text{FOI}(t)\Delta S(t)}{\text{FOI}(t) + \mu} \quad (\text{S87})$$

$$\Delta I(t) = [1 - \exp(-(\gamma + \mu)\Delta t)] I(t - \Delta t) \quad (\text{S88})$$

$$N_{IR}(t) = \frac{\gamma \Delta I(t)}{\gamma + \mu} \quad (\text{S89})$$

$$\Delta R(t) = [1 - \exp(-(\nu + \mu)\Delta t)] R(t - \Delta t) \quad (\text{S90})$$

$$N_{RS}(t) = \frac{\nu \Delta R(t)}{\nu + \mu} \quad (\text{S91})$$

$$S(t) = S(t - \Delta t) + \mu S - \Delta S(t) + N_{RS}(t) \quad (\text{S92})$$

$$I(t) = I(t - \Delta t) - \Delta I(t) + N_{SI}(t) \quad (\text{S93})$$

$$R(t) = R(t - \Delta t) - \Delta R(t) + N_{IR}(t) \quad (\text{S94})$$

661 where we include an extra term ω to account for external infections. Although actual
662 simulations did not include any external infections, we found that including this term
663 generally helped with model convergence in previous analyses [4]. The transmission
664 rate was divided into a seasonal term $\beta_{\text{seas}}(t)$ (repeated every year) and intervention
665 term $\alpha(t)$, which were estimated jointly:

$$\beta(t) = \beta_{\text{seas}}(t)\alpha(t), \quad (\text{S95})$$

666 where $\alpha < 1$ corresponds to reduction in transmission due to intervention effects. To
667 constrain the smoothness of $\beta_{\text{seas}}(t)$, we imposed cyclic, random-walk priors:

$$\beta_{\text{seas}}(t) \sim \text{Normal}(\beta_{\text{seas}}(t - 1), \sigma) \quad t = 2 \dots 52 \quad (\text{S96})$$

$$\beta_{\text{seas}}(1) \sim \text{Normal}(\beta_{\text{seas}}(52), \sigma) \quad (\text{S97})$$

668 [SWP: I noticed that I forgot to put a prior on σ so need to re-do this but won't
 669 change the results.] We fixed $\alpha(t) = 1$ for all $t < 2020$ and estimate α assuming a
 670 normal prior:

$$\alpha \sim \text{Normal}(1, 0.25). \quad (\text{S98})$$

671 We assumed weakly informative priors on ω and ν :

$$\omega \sim \text{Normal}(0, 200) \quad (\text{S99})$$

$$\nu \sim \text{Normal}(104, 26) \quad (\text{S100})$$

672 We assumed that the true birth/death rates, population sizes, and recovery rates are
 673 known. We note, however, that assuming $\gamma = 1/\text{week}$ actually corresponds to a mean
 674 simulated infectious period of 1.6 weeks, which is much longer than the true value;
 675 this approximation allows us to test whether we can still robustly estimate the in-
 676 trinsic resilience given parameter mis-specification. Initial conditions were estimated
 677 with following priors:

$$S(0) = Ns(0) \quad (\text{S101})$$

$$I(0) = Ni(0) \quad (\text{S102})$$

$$s(0) \sim \text{Uniform}(0, 1) \quad (\text{S103})$$

$$i(0) \sim \text{Half-Normal}(0, 0.001) \quad (\text{S104})$$

678 Finally, the observation model was specified as follows:

$$\text{Cases}(t) \sim \text{Negative-Binomial}(\rho N_{SI}(t), \phi) \quad (\text{S105})$$

$$\rho \sim \text{Half-Normal}(0, 0.02) \quad (\text{S106})$$

$$\phi \sim \text{Half-Normal}(0, 10) \quad (\text{S107})$$

679 where ρ represents the reporting probability and ϕ represents the negative binomial
 680 overdispersion parameter.

681 The model was fitted to four separate time series: (1) incidence time series from
 682 the SIRS model, (2) incidence time series for strain 1 from the two-strain model,
 683 (3) incidence time series for strain 2 from the two-strain model, and (4) combined
 684 incidence time series for strains 1 and 2 from the two-strain model. The model was
 685 fitted using rstan [34, 35]. The resulting posterior distribution was used to calculate
 686 the intrinsic resilience of the seasonally unforced system with the same parameters;
 687 eigenvalues of the discrete-time SIR model were computed by numerically finding
 688 the equilibrium and calculating the Jacobian matrix.

689 Validations for window-selection criteria

690 We used stochastic SIRS simulations to identify optimal parameters for the window-
 691 selection criteria that we used for the linear regression for estimating empirical re-
 692 silience. For each simulation, we began by generating a random perturbation $\alpha(t)$

693 from a random set of parameters. First, we drew the duration of intervention τ_{npi}
 694 from a uniform distribution between 1 and 2 years. Then, we drew independent
 695 normal variables z_i of length $\lfloor 364\tau_{\text{npi}} \rfloor$ with a standard deviation of 0.02 and took a
 696 reverse cumulative sum to obtain a realistic shape for the intervention:

$$x_n = 1 + \sum_{i=n}^{\lfloor 364\tau_{\text{npi}} \rfloor} z_i, \quad n = 1, \dots, \lfloor 364\tau_{\text{npi}} \rfloor. \quad (\text{S108})$$

697 We repeated this random generation process until less than 10% of x_n exceeds 1—
 698 this was done to prevent the perturbation $\alpha(t)$ stays below 1 (and therefore reduce
 699 transmission) for the most part. Then, we set any values that are above 1 or below 0
 700 as 1 and 0, respectively. Then, we randomly drew the minimum transmission during
 701 intervention α_{\min} from a uniform distribution between 0.5 and 0.7 and scale x_n to
 702 have a minimum of α_{\min} :

$$x_{\text{scale},n} = \alpha_{\min} + (1 - \alpha_{\min}) \times \frac{x_n - \min x_n}{1 - \min x_n}. \quad (\text{S109})$$

703 This allowed us to simulate a realistically shaped intervention:

$$\alpha(t) = \begin{cases} 1 & t < 2020 \\ x_{\text{scale},364(t-2020)} & 2020 \leq t < 2020 + \tau_{\text{npi}} \\ 1 & \tau_{\text{npi}} \leq t \end{cases}. \quad (\text{S110})$$

704 Given this intervention function, we draw \mathcal{R}_0 from a uniform distribution between 1.5
 705 and 4 and the mean duration of immunity $1/\delta$ from a uniform distribution between
 706 1 and 4. Then, we simulate the stochastic SIRS model from $S(0) = 10^8/\mathcal{R}_0$ and
 707 $I(0) = 100$ from 1990 to 2025 and truncate the time series to 2014–2025; if the
 708 epidemic becomes extinct before the end of simulation, we discard that simulation
 709 and start over from the intervention generation step.

710 For each epidemic simulation, we computed the empirical resilience by varying
 711 the threshold R for the nearest neighbor approach from 4 to 14 with increments of
 712 2, the number of divisions K for the window selection between 8 and 25, and the
 713 truncation threshold a for the window selection between 1 to 3; this was done for all
 714 possible combinations of R , K , and a . We also compared this with the naive approach
 715 that uses the entire distance-from-attractor time series, starting from the maximum
 716 distance to the end of the time series. We repeated this procedure 500 times and
 717 quantified the correlation between empirical and intrinsic resilience estimates across
 718 two approaches.

⁷¹⁹ **Supplementary Figures**

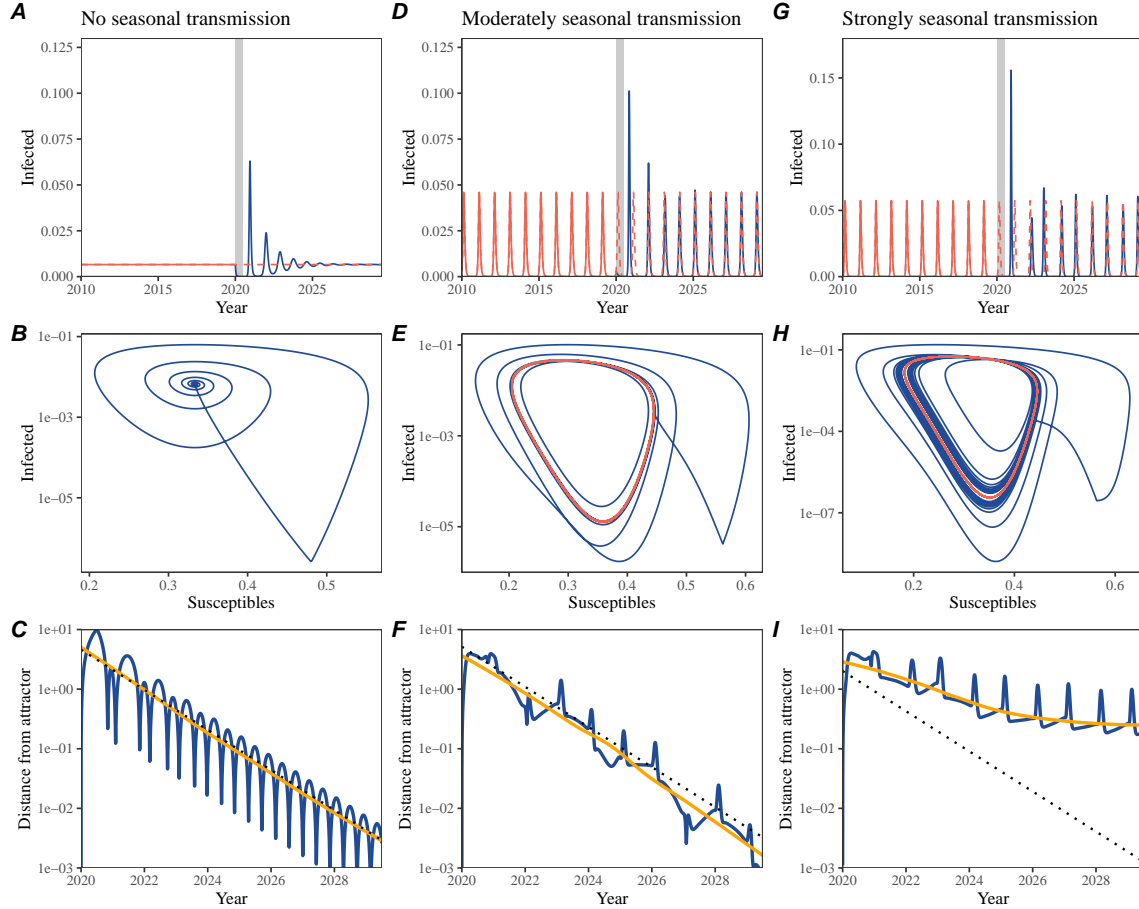


Figure S1: Impact of seasonal transmission on pathogen resilience. (A, D, G) Simulated epidemic trajectories using the SIRS model without seasonal forcing (A), with seasonal forcing of amplitude of 0.2 (D), and with seasonal forcing of amplitude of 0.4 (G). Red and blue solid lines represent epidemic dynamics before and after interventions are introduced, respectively. Red dashed lines represent counterfactual epidemic dynamics in the absence of interventions. Gray regions indicate the duration of interventions. (B, E, H) Phase plane representation of the time series in panels A, D, and G alongside the corresponding susceptible host dynamics. Red and blue solid lines represent epidemic trajectories on an SI phase plane before and after interventions are introduced, respectively. (C, F, I) Changes in logged distance from the attractor over time. Blue lines represent the logged distance from the attractor. Orange lines represent the locally estimated scatterplot smoothing (LOESS) fits to the logged distance from the attractor. Dotted lines show the intrinsic resilience of the seasonally unforced system.

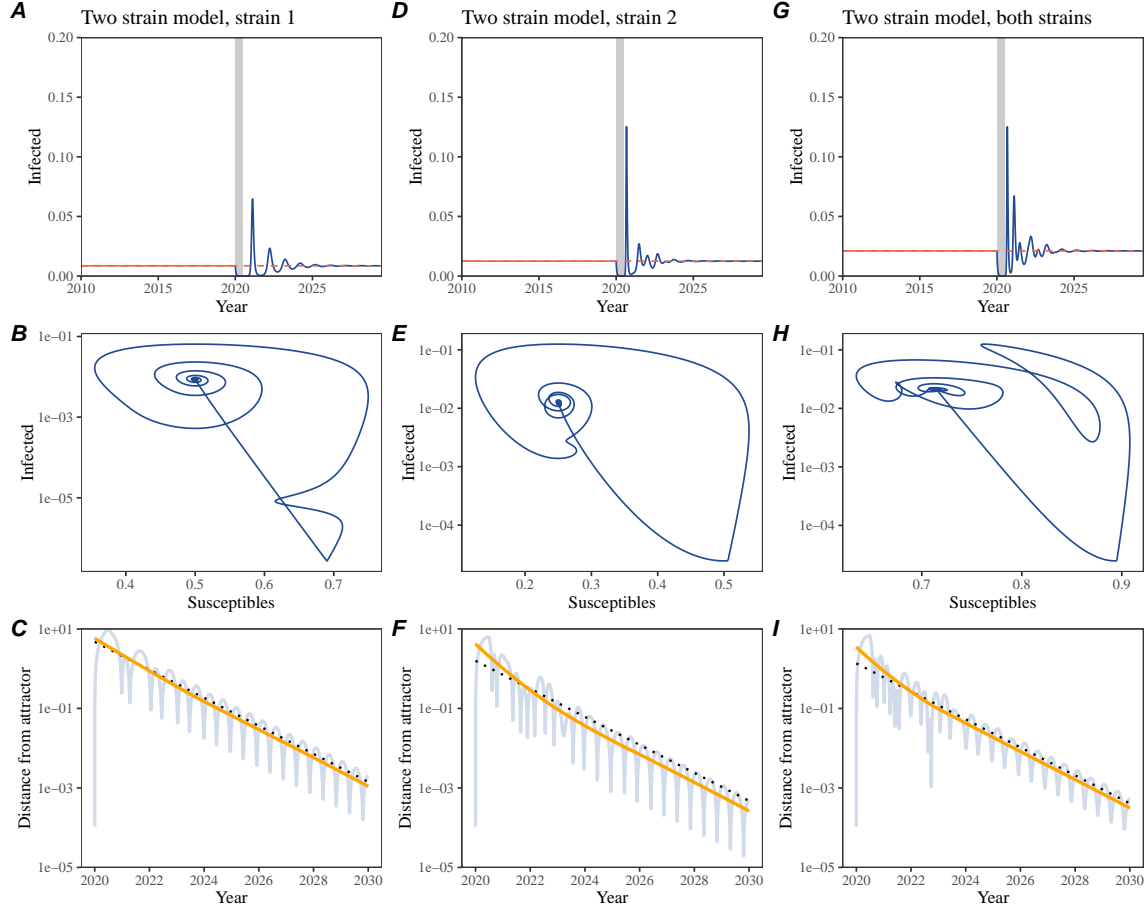


Figure S2: Conceptual framework for measuring pathogen resilience following NPIs for a two-strain system without seasonal forcing. (A, D, G) Simulated epidemic trajectories using a multi-strain system without seasonal forcing. Red and blue solid lines represent epidemic dynamics before and after interventions are introduced, respectively. Red dashed lines represent counterfactual epidemic dynamics in the absence of interventions. Gray regions indicate the duration of interventions. (B, E, H) Phase plane representation of the time series in panels A, D, and G alongside the corresponding susceptible host dynamics. Blue solid lines represent epidemic trajectories on an SI phase plane before and after interventions are introduced, respectively. (C, F, I) Changes in logged distance from the attractor over time. Blue lines represent the logged distance from the attractor. Orange lines represent the locally estimated scatterplot smoothing (LOESS) fits to the logged distance from the attractor. Dotted lines show the intrinsic resilience of the seasonally unforced system.

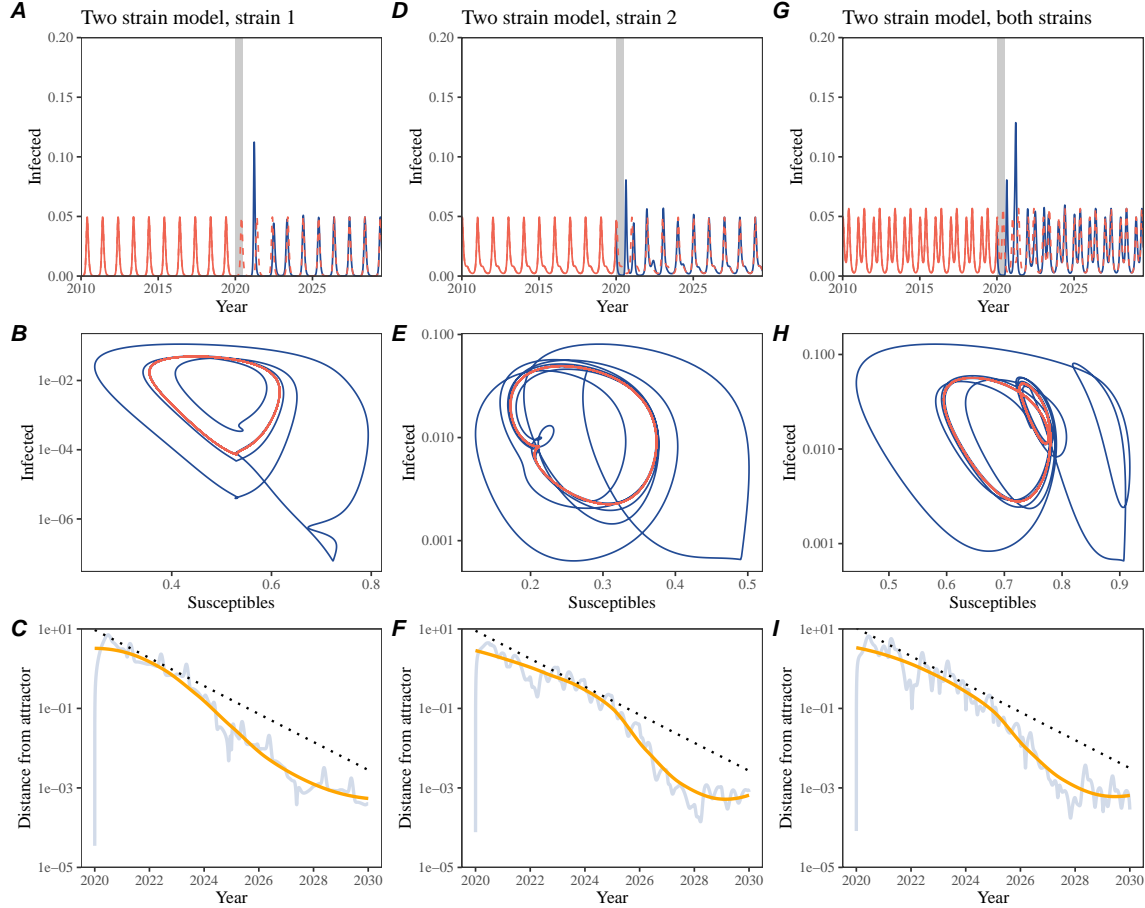


Figure S3: Conceptual framework for measuring pathogen resilience following NPIs for a two-strain system with seasonal forcing. (A, D, G) Simulated epidemic trajectories using a two-strain system with seasonal forcing (amplitude of 0.2). In this model, two strains compete through cross immunity. Red and blue solid lines represent epidemic dynamics before and after interventions are introduced, respectively. Red dashed lines represent counterfactual epidemic dynamics in the absence of interventions. Gray regions indicate the duration of interventions. (B, E, H) Phase plane representation of the time series in panels A, D, and G alongside the corresponding susceptible host dynamics. Red and blue solid lines represent epidemic trajectories on an SI phase plane before and after interventions are introduced, respectively. (C, F, I) Changes in logged distance from the attractor over time. Blue lines represent the logged distance from the attractor. Orange lines represent the locally estimated scatterplot smoothing (LOESS) fits to the logged distance from the attractor. Dotted lines show the intrinsic resilience of the seasonally unforced system.

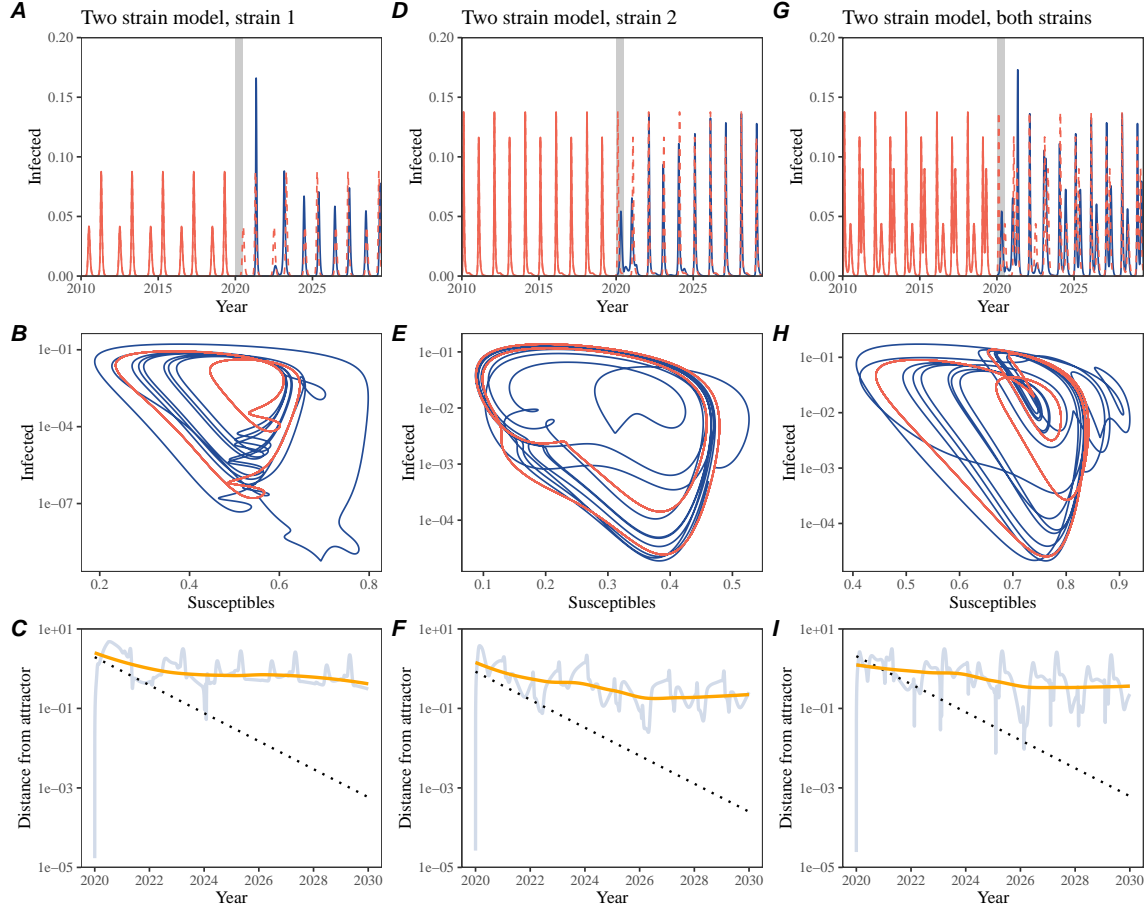


Figure S4: Conceptual framework for measuring pathogen resilience following NPIs for a multi-strain system with strong seasonal forcing. (A, D, G) Simulated epidemic trajectories using a multi-strain system with seasonal forcing (amplitude of 0.4). In this model, two strains compete through cross immunity. Red and blue solid lines represent epidemic dynamics before and after interventions are introduced, respectively. Red dashed lines represent counterfactual epidemic dynamics in the absence of interventions. Gray regions indicate the duration of interventions. (B, E, H) Phase plane representation of the time series in panels A, D, and G alongside the corresponding susceptible host dynamics. Red and blue solid lines represent epidemic trajectories on an SI phase plane before and after interventions are introduced, respectively. (C, F, I) Changes in logged distance from the attractor over time. Blue lines represent the logged distance from the attractor. Orange lines represent the locally estimated scatterplot smoothing (LOESS) fits to the logged distance from the attractor. Dotted lines show the intrinsic resilience of the seasonally unforced system.

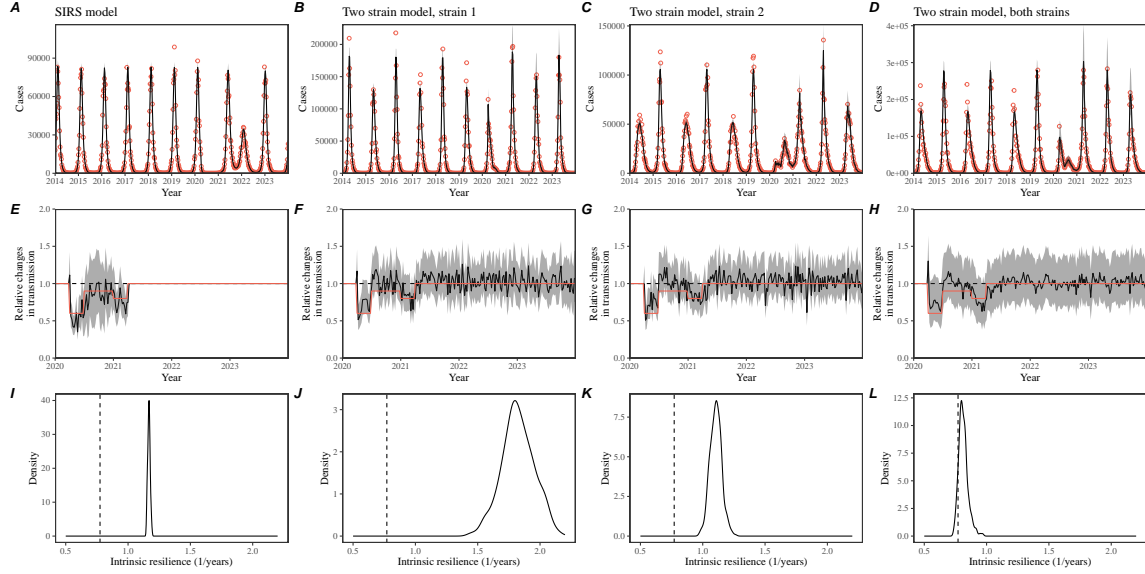


Figure S5: Mechanistic model fits to simulated data and inferred intrinsic resilience. We simulated discrete time, stochastic epidemic trajectories using seasonally forced SIRS model (A,E,I) and seasonally forced two-strain model (B–D, F–H, and J–L) and tested whether we can estimate the intrinsic resilience of the seasonally unforced versions of the model by fitting a mechanistic model (Supplementary Text). We fitted the same discrete time, deterministic SIRS model across all four scenarios. (A–D) Simulated case time series from corresponding models shown in the title (red) and SIRS model fits (black). (E–H) Assumed changes in transmission due to pandemic perturbations (red) and estimated time-varying relative transmission rates for the perturbation impact from the SIRS model fits (black). Solid lines and shaded regions represent fitted posterior median and 95% credible intervals. (I–L) True intrinsic resilience of the seasonally unforced system (vertical lines) and the posterior distribution of the inferred intrinsic resilience from the SIRS model (density plots).

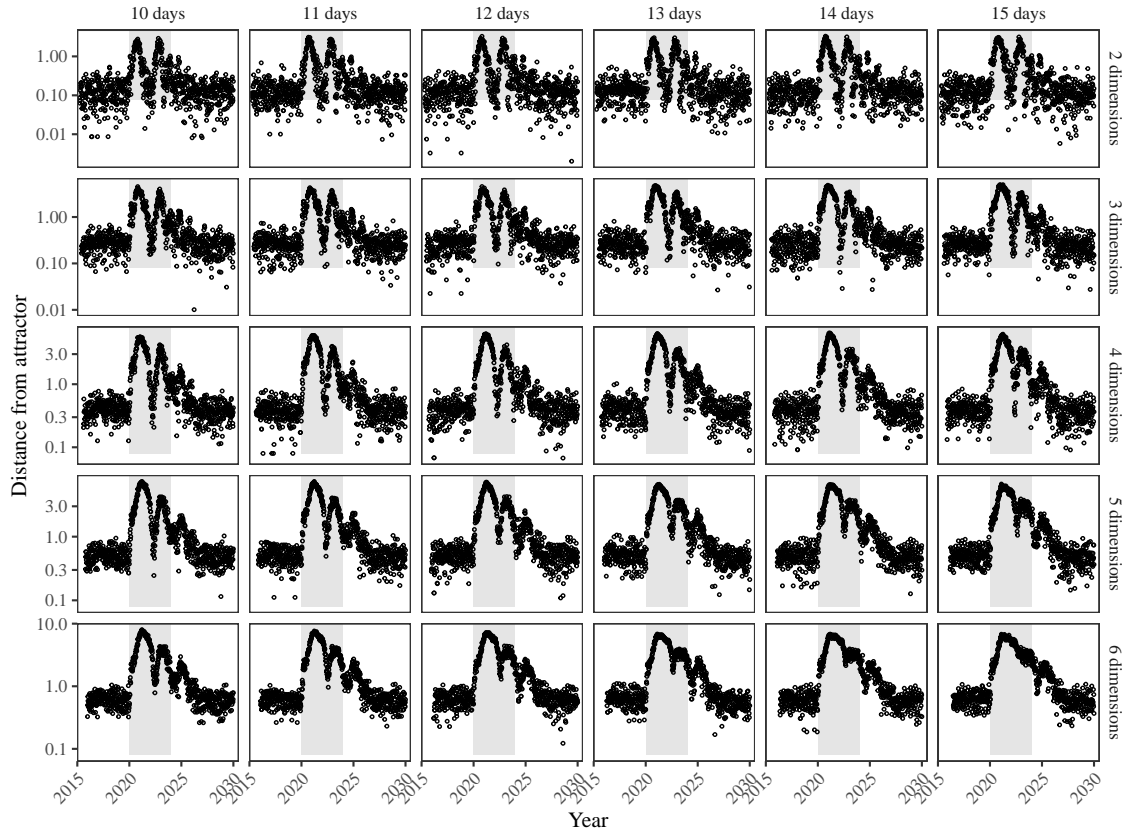


Figure S6: Sensitivity of the distance from the attractor to choices about embedding lags and dimensions. Sensitivity analysis for the distance-from-attractor time series shown in Figure 3E in the main text by varying the embedding lag between 10–15 days and embedding dimensions between 2–6 dimensions. [SWP: You said: “Did you do sensitivity analyses with other systems or just this one? I think we’ll probably need to do it with several systems”. I think it’s OK to just do this because we’re just trying to show qualitatively that longer lags and higher dimensions smooth things out. We also explore resilience of other models in other figures.]

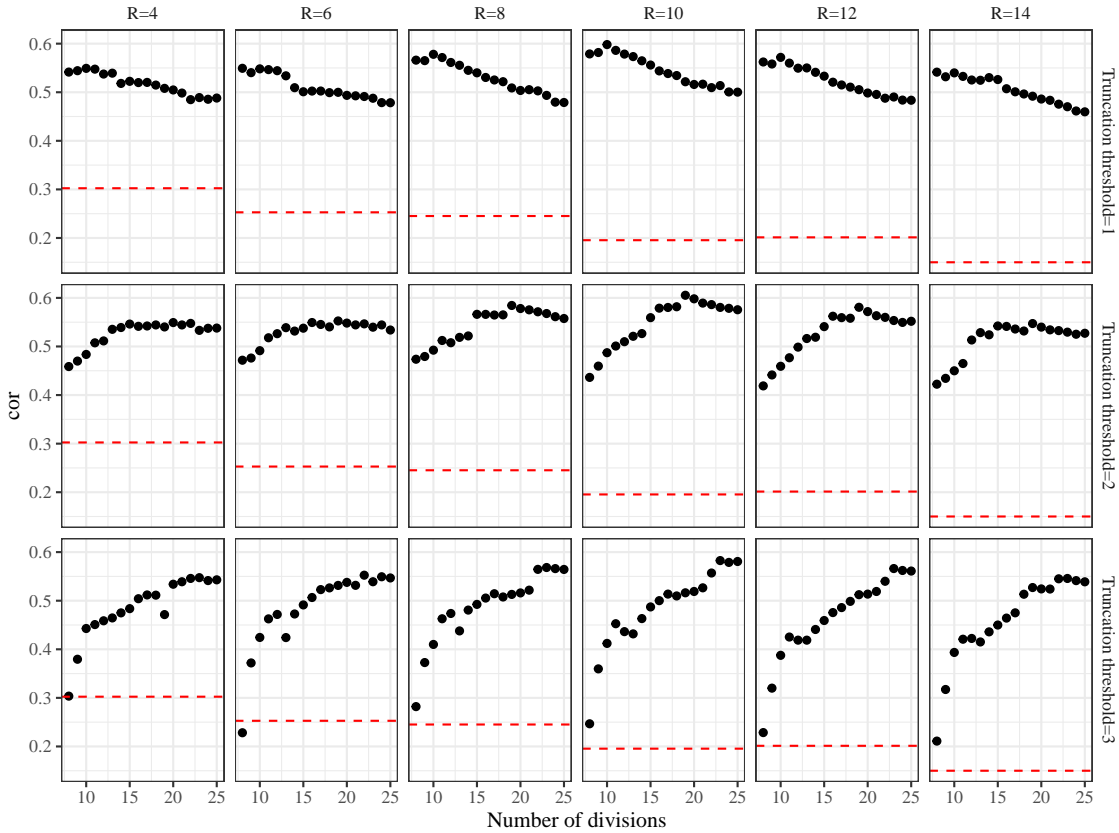


Figure S7: Impact of fitting window selection on the estimation of empirical resilience. We simulated 500 epidemics of a stochastic SIRS model with randomly drawn parameters and randomly generated pandemic perturbations (Supplementary Text). For each simulation, we varied the false nearest neighbor threshold R for reconstructing the empirical attractor as well as the parameters for regression window selection (i.e., the truncation threshold a and the the number of divisions K). Each point represents the resulting correlation coefficient between empricial and intrinsic resilience estimates for a given scenario. Dashed lines represent the correlation coefficient between empricial and intrinsic resilience estimates for the naive approach that fits a linear regression on a log scale, starting from the maximum distance until the end of the time series.

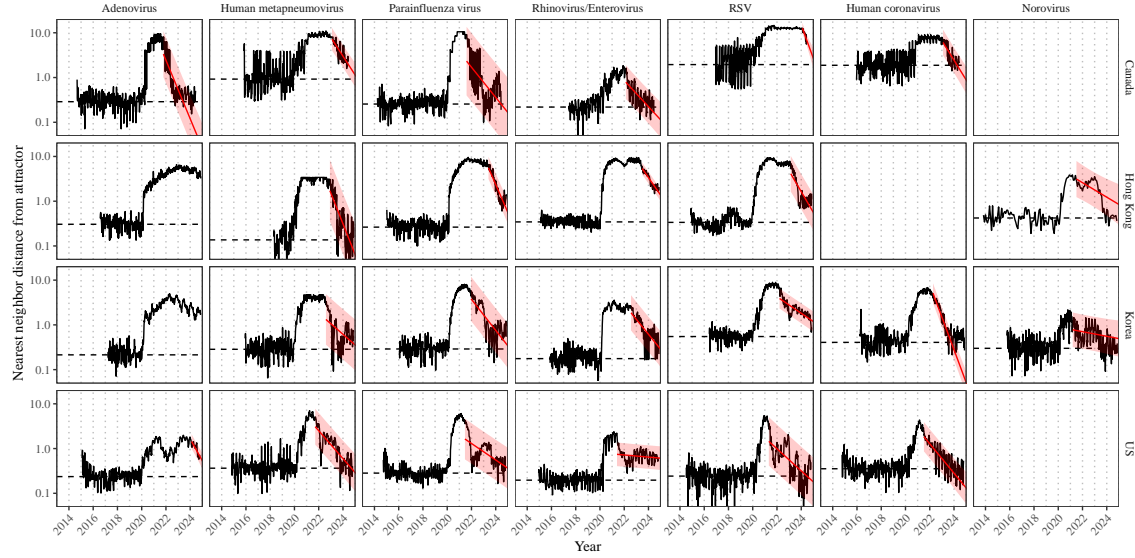


Figure S8: Estimated time series of distance from the attractor for each pathogen and corresponding linear regression fits using automated window selection criterion across Canada, Hong Kong, Korea, and the US. Black lines represent the estimated distance from the attractor. Red lines and shaded regions represent the linear regression fits and corresponding 95% confidence intervals. Dashed lines represent the average of the pre-pandemic nearest neighbor distances.

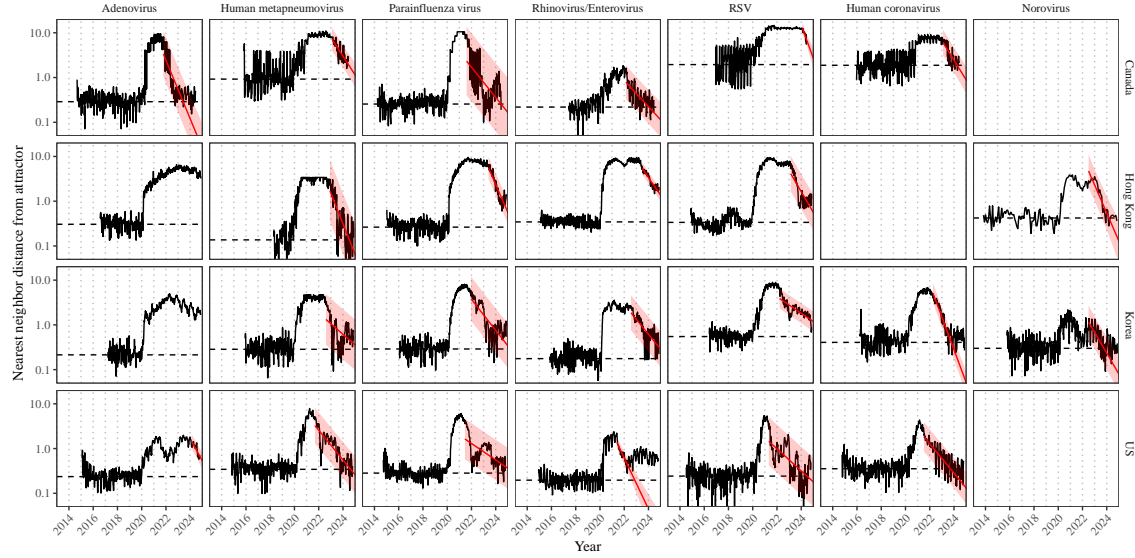


Figure S9: Estimated time series of distance from the attractor for each pathogen and corresponding linear regression fits across Canada, Hong Kong, Korea, and the US, including ad-hoc regression window selection. We used ad-hoc regression windows for norovirus in Hong Kong and Korea and Rhinovirus/Enterovirus in the US. Black lines represent the estimated distance from the attractor. Red lines and shaded regions represent the linear regression fits and corresponding 95% confidence intervals. Dashed lines represent the average of the pre-pandemic nearest neighbor distances.

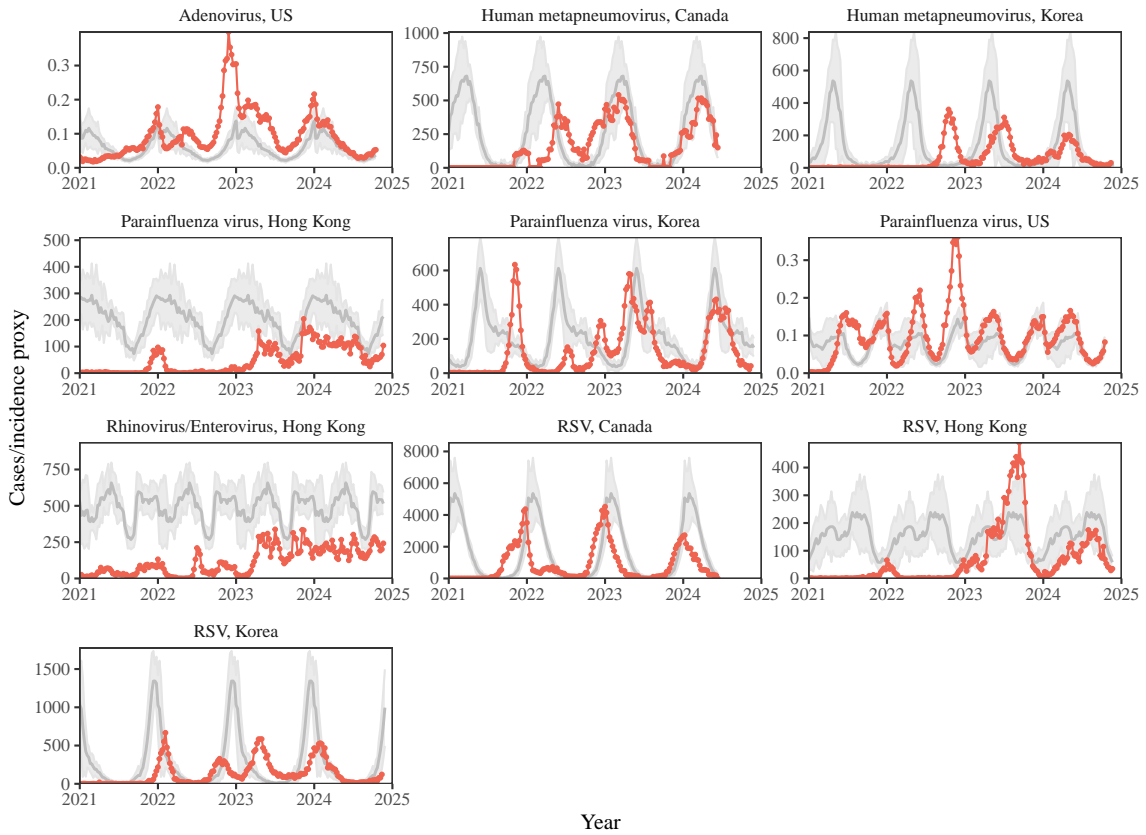


Figure S10: Observed dynamics for pathogen that are predicted to return after the end of 2024. Red points and lines represent data before 2020. Gray lines and shaded regions represent the mean seasonal patterns and corresponding 95% confidence intervals around the mean, previously shown in Figure 1.

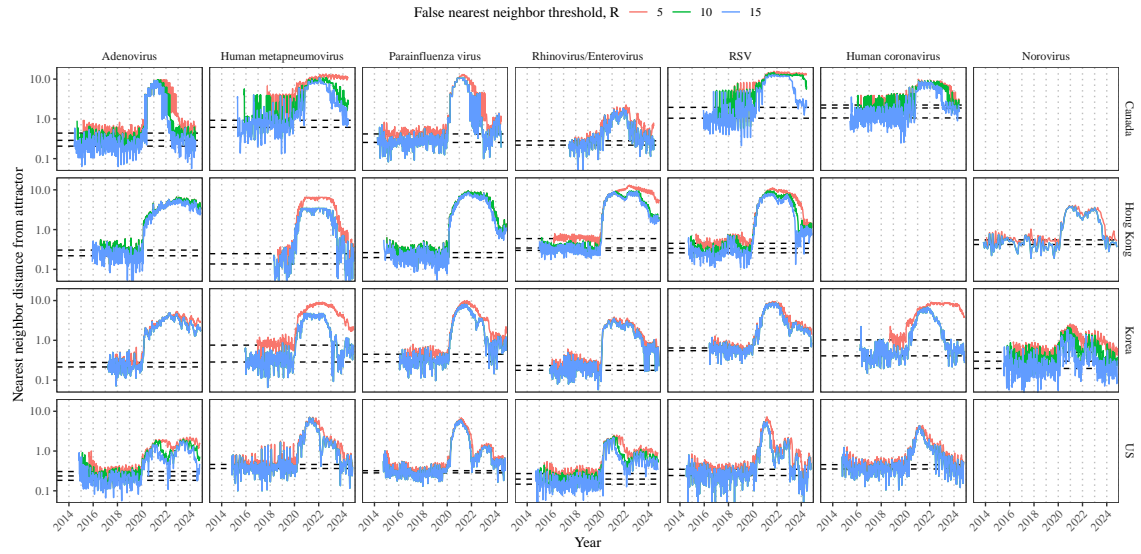


Figure S11: Estimated time series of distance from the attractor for each pathogen across different choices about false nearest neighbor threshold values. Using higher threshold values for the false nearest neighbor approach gives lower embedding dimensions. Colored lines represent the estimated distance from the attractor for different threshold values.

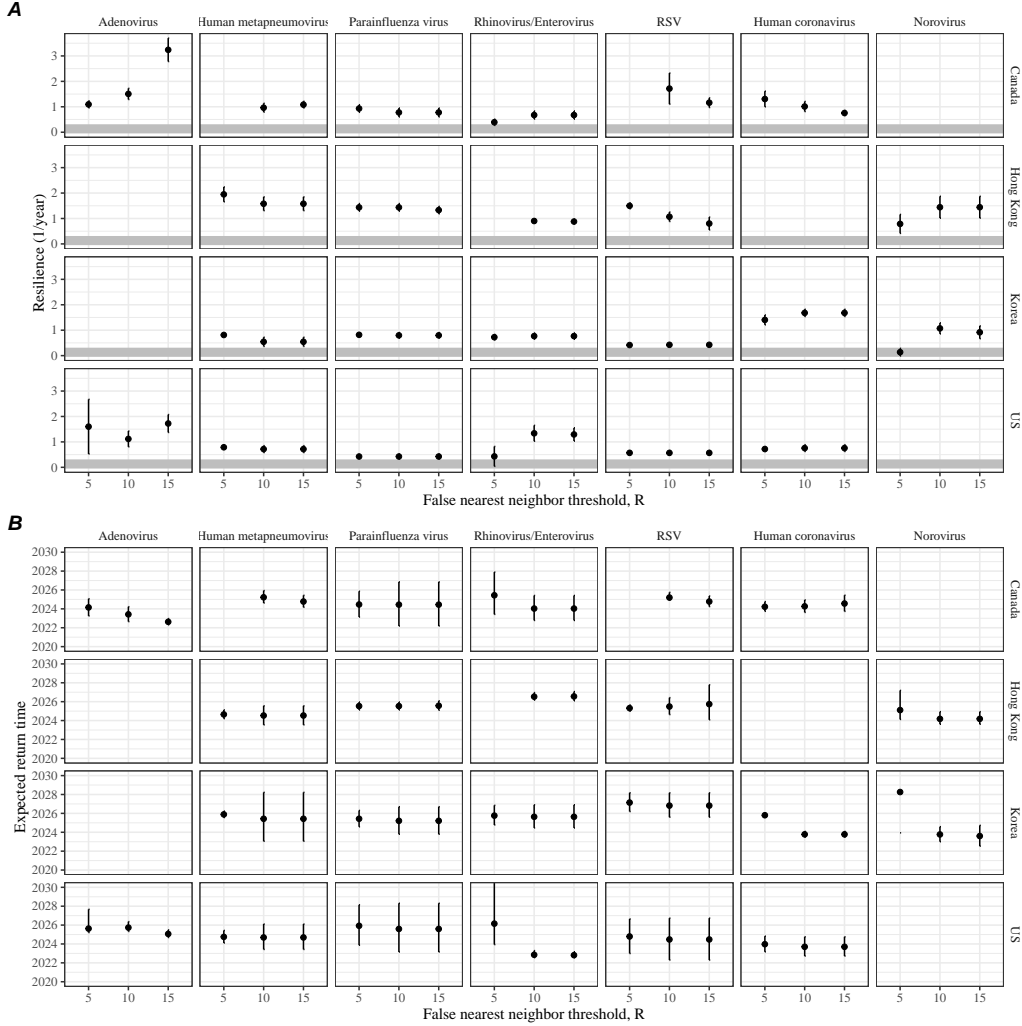


Figure S12: Summary of resilience estimates and predictions for return time across different choices about false nearest neighbor threshold values. The automated window selection method was used for all scenarios to estimate pathogen resilience, except for norovirus in Hong Kong and Korea and Rhinovirus/Enterovirus in the US. We used the same ad-hoc regression windows for norovirus in Hong Kong and Korea and Rhinovirus/Enterovirus in the US as we did in the main analysis. (A) Estimated pathogen resilience. The gray horizontal line represents the intrinsic resilience of pre-vaccination measles dynamics. (B) Predicted timing of when each pathogen will return to their pre-pandemic cycles. The dashed line in panel B indicates the end of 2024 (current observation time). Error bars represent 95% confidence intervals.

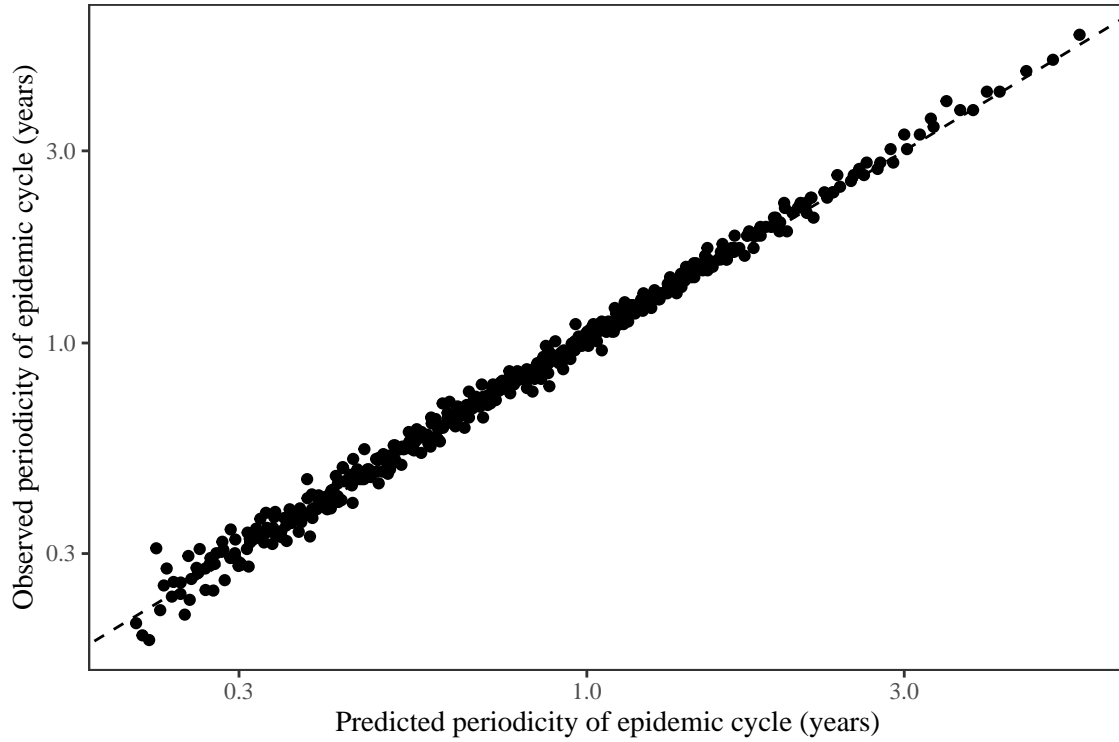


Figure S13: **Comparison between the observed and predicted periodicity of the epidemic cycle of the seasonally unforced SIRS model.** The observed periodicity of the epidemic corresponds to the periodicity at which maximum spectral density occurs. The predicted periodicity of the epidemic corresponds to $2\pi/\text{Im}(\lambda)$, where $\text{Im}(\lambda)$ is the imaginary part of the eigenvalue.

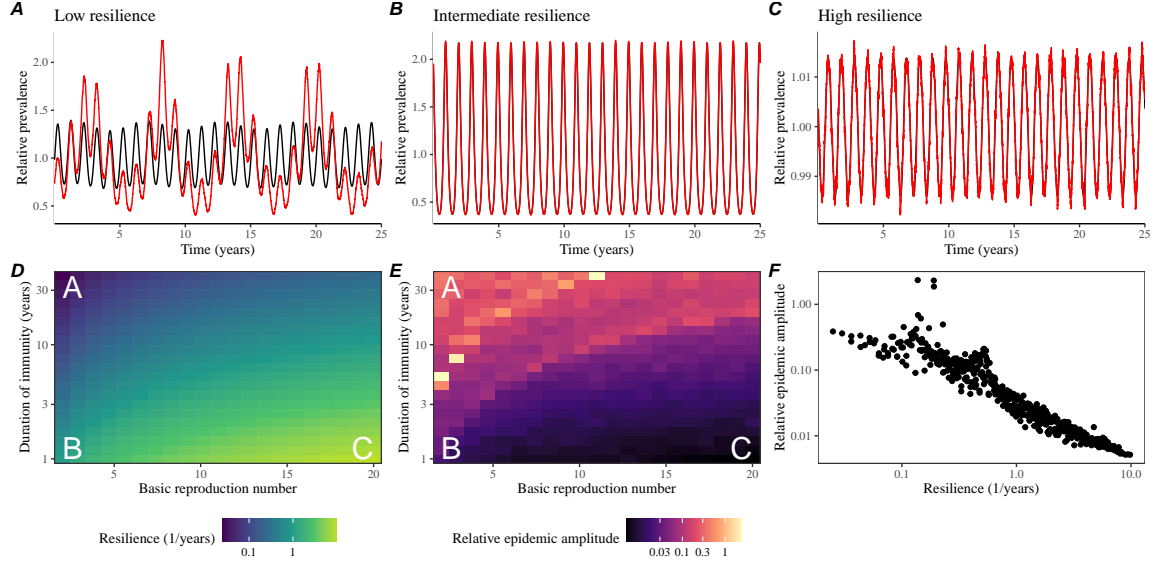


Figure S14: Linking resilience of a host-pathogen system to its sensitivity to stochastic perturbations for the seasonally forced SIRS model. (A–C) Epidemic trajectories of a stochastic SIRS model across three different resilience values: low, intermediate, and high. The relative prevalence was calculated by dividing infection prevalence by its mean value. (D) The heat map represents the intrinsic resilience of the seasonally unforced system as a function of the basic reproduction number \mathcal{R}_0 and the duration of immunity. (E) The heat map represents the relative epidemic amplitude as a function of the basic reproduction number \mathcal{R}_0 and the duration of immunity. To calculate the relative epidemic amplitude, we first take the relative difference in infection prevalence between stochastic and deterministic trajectories: $\epsilon = (I_{\text{stoch}} - I_{\text{det}})/I_{\text{det}}$. Then, we calculate the difference between maximum and minimum of the relative difference and divide by half: $(\max \epsilon - \min \epsilon)/2$. (F) The relationship between pathogen resilience and relative epidemic amplitude.

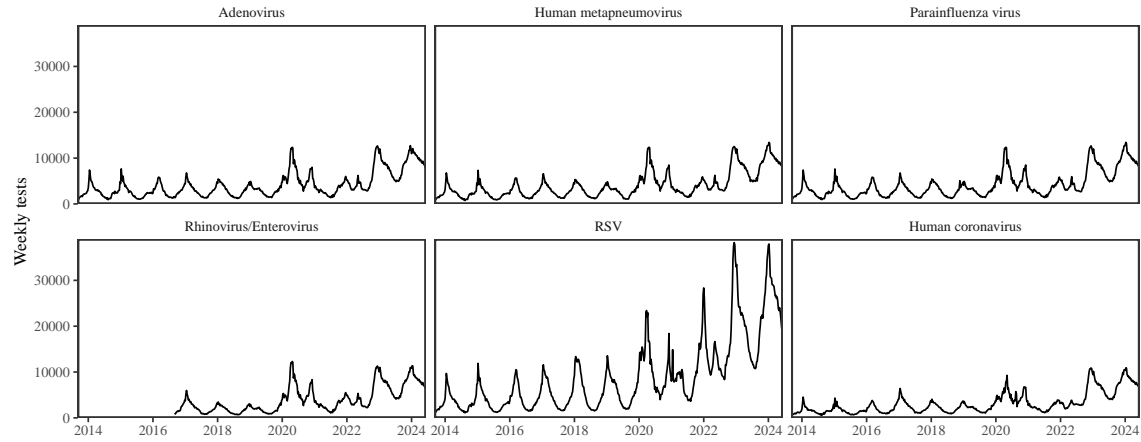


Figure S15: Testing patterns for respiratory pathogens in Canada.

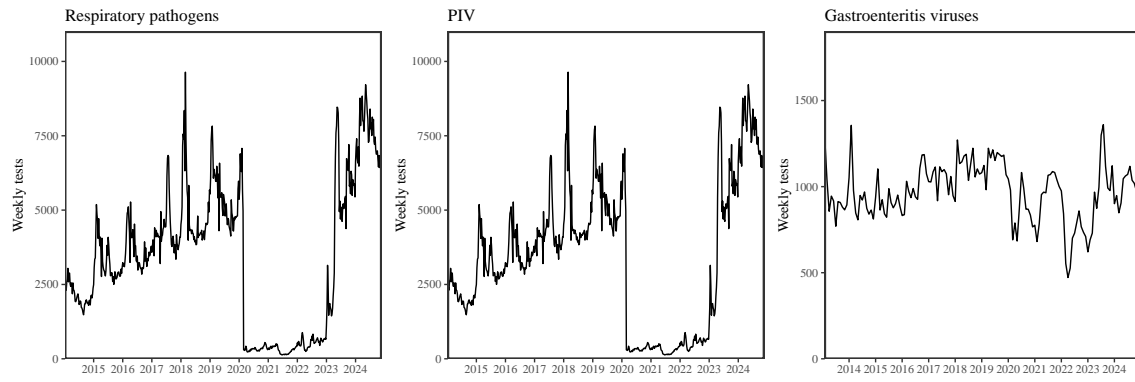


Figure S16: Testing patterns for respiratory pathogens, PIV, and gastroenteritis viruses in Hong Kong.

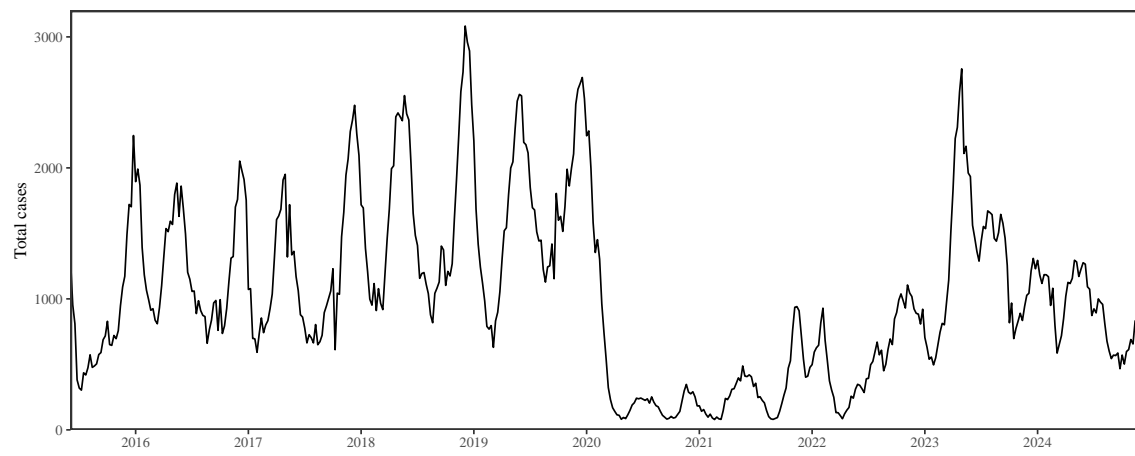


Figure S17: Total number of reported respiratory infection cases in Korea.

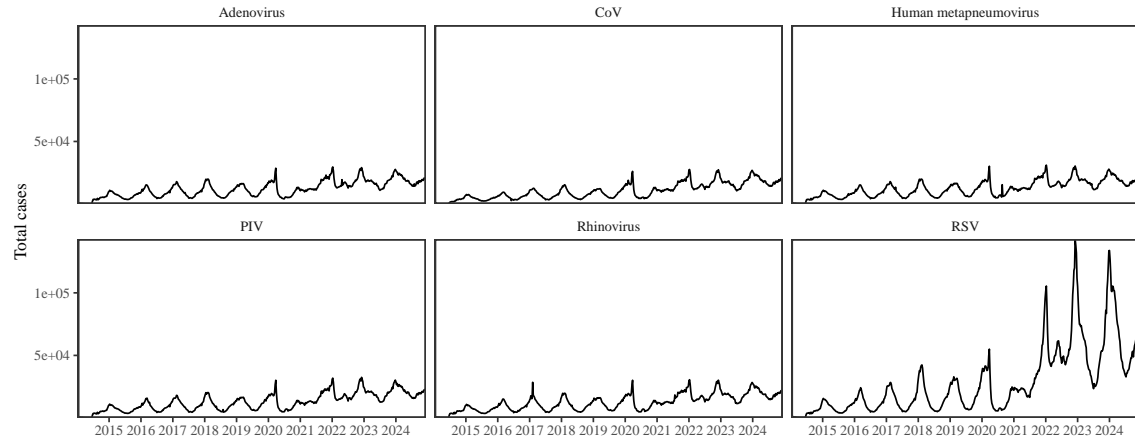


Figure S18: Testing patterns for respiratory pathogens in the US reported through the NREVSS.

720 **References**

- 721 [1] Rachel E Baker, Sang Woo Park, Wenchang Yang, Gabriel A Vecchi, C Jessica E
722 Metcalf, and Bryan T Grenfell. The impact of COVID-19 nonpharmaceutical
723 interventions on the future dynamics of endemic infections. *Proceedings of the*
724 *National Academy of Sciences*, 117(48):30547–30553, 2020.
- 725 [2] Gabriela B Gomez, Cedric Mahé, and Sandra S Chaves. Uncertain effects of the
726 pandemic on respiratory viruses. *Science*, 372(6546):1043–1044, 2021.
- 727 [3] Mihaly Koltai, Fabienne Krauer, David Hodgson, Edwin van Leeuwen, Marina
728 Treskova-Schwarzbach, Mark Jit, and Stefan Flasche. Determinants of RSV
729 epidemiology following suppression through pandemic contact restrictions. *Epi-*
730 *demics*, 40:100614, 2022.
- 731 [4] Sang Woo Park, Brooklyn Noble, Emily Howerton, Bjarke F Nielsen, Sarah
732 Lentz, Lilliam Ambroggio, Samuel Dominguez, Kevin Messacar, and Bryan T
733 Grenfell. Predicting the impact of non-pharmaceutical interventions against
734 COVID-19 on *Mycoplasma pneumoniae* in the United States. *Epidemics*,
735 49:100808, 2024.
- 736 [5] Amanda C Perofsky, Chelsea L Hansen, Roy Burstein, Shanda Boyle, Robin
737 Prentice, Cooper Marshall, David Reinhart, Ben Capodanno, Melissa Truong,
738 Kristen Schwabe-Fry, et al. Impacts of human mobility on the citywide trans-
739 mission dynamics of 18 respiratory viruses in pre-and post-COVID-19 pandemic
740 years. *Nature communications*, 15(1):4164, 2024.
- 741 [6] Eric J Chow, Timothy M Uyeki, and Helen Y Chu. The effects of the COVID-19
742 pandemic on community respiratory virus activity. *Nature Reviews Microbiol-*
743 *ogy*, 21(3):195–210, 2023.
- 744 [7] Stephen M Kissler, Christine Tedijanto, Edward Goldstein, Yonatan H Grad,
745 and Marc Lipsitch. Projecting the transmission dynamics of SARS-CoV-2
746 through the postpandemic period. *Science*, 368(6493):860–868, 2020.
- 747 [8] Rachel E Baker, Chadi M Saad-Roy, Sang Woo Park, Jeremy Farrar, C Jessica E
748 Metcalf, and Bryan T Grenfell. Long-term benefits of nonpharmaceutical inter-
749 ventions for endemic infections are shaped by respiratory pathogen dynamics.
750 *Proceedings of the National Academy of Sciences*, 119(49):e2208895119, 2022.
- 751 [9] John-Sebastian Eden, Chisha Sikazwe, Ruopeng Xie, Yi-Mo Deng, Sheena G
752 Sullivan, Alice Michie, Avram Levy, Elena Cutmore, Christopher C Blyth,
753 Philip N Britton, et al. Off-season RSV epidemics in Australia after easing
754 of COVID-19 restrictions. *Nature communications*, 13(1):2884, 2022.
- 755 [10] Stuart L Pimm. The structure of food webs. *Theoretical population biology*,
756 16(2):144–158, 1979.

- 757 [11] Michael G Neubert and Hal Caswell. Alternatives to resilience for measuring
758 the responses of ecological systems to perturbations. *Ecology*, 78(3):653–665,
759 1997.
- 760 [12] Lance H Gunderson. Ecological resilience—in theory and application. *Annual
761 review of ecology and systematics*, 31(1):425–439, 2000.
- 762 [13] Vasilis Dakos and Sonia Kéfi. Ecological resilience: what to measure and how.
763 *Environmental Research Letters*, 17(4):043003, 2022.
- 764 [14] Floris Takens. Detecting strange attractors in turbulence. In *Dynamical Sys-
765 tems and Turbulence, Warwick 1980: proceedings of a symposium held at the
766 University of Warwick 1979/80*, pages 366–381. Springer, 2006.
- 767 [15] Jonathan Dushoff, Joshua B Plotkin, Simon A Levin, and David JD Earn. Dynamical resonance can account for seasonality of influenza epidemics. *Pro-
768 ceedings of the National Academy of Sciences*, 101(48):16915–16916, 2004.
- 770 [16] Alan Hastings, Karen C Abbott, Kim Cuddington, Tessa Francis, Gabriel Gell-
771 ner, Ying-Cheng Lai, Andrew Morozov, Sergei Petrovskii, Katherine Scran-
772 ton, and Mary Lou Zeeman. Transient phenomena in ecology. *Science*,
773 361(6406):eaat6412, 2018.
- 774 [17] Matthew B Kennel, Reggie Brown, and Henry DI Abarbanel. Determining
775 embedding dimension for phase-space reconstruction using a geometrical con-
776 struction. *Physical review A*, 45(6):3403, 1992.
- 777 [18] Eugene Tan, Shannon Algar, Débora Corrêa, Michael Small, Thomas Stemler,
778 and David Walker. Selecting embedding delays: An overview of embedding
779 techniques and a new method using persistent homology. *Chaos: An Interdis-
780 ciplinary Journal of Nonlinear Science*, 33(3), 2023.
- 781 [19] Jennifer M Radin, Anthony W Hawksworth, Peter E Kammerer, Melinda Bal-
782 ansay, Rema Raman, Suzanne P Lindsay, and Gary T Brice. Epidemiology
783 of pathogen-specific respiratory infections among three US populations. *PLoS
784 One*, 9(12):e114871, 2014.
- 785 [20] Guojian Lv, Limei Shi, Yi Liu, Xuecheng Sun, and Kai Mu. Epidemiological
786 characteristics of common respiratory pathogens in children. *Scientific Reports*,
787 14(1):16299, 2024.
- 788 [21] Saverio Caini, Adam Meijer, Marta C Nunes, Laetitia Henaff, Malaika Zounon,
789 Bronke Boudewijns, Marco Del Riccio, and John Paget. Probable extinction of
790 influenza b/yamagata and its public health implications: a systematic literature
791 review and assessment of global surveillance databases. *The Lancet Microbe*,
792 2024.

- 793 [22] Zhiyuan Chen, Joseph L-H Tsui, Bernardo Gutierrez, Simon Busch Moreno,
794 Louis du Plessis, Xiaowei Deng, Jun Cai, Sumali Bajaj, Marc A Suchard,
795 Oliver G Pybus, et al. COVID-19 pandemic interventions reshaped the global
796 dispersal of seasonal influenza viruses. *Science*, 386(6722):eadq3003, 2024.
- 797 [23] Bryan T Grenfell, Ottar N Bjørnstad, and Bärbel F Finkenstädt. Dynamics of
798 measles epidemics: scaling noise, determinism, and predictability with the TSIR
799 model. *Ecological monographs*, 72(2):185–202, 2002.
- 800 [24] Samit Bhattacharyya, Per H Gesteland, Kent Korgenski, Ottar N Bjørnstad,
801 and Frederick R Adler. Cross-immunity between strains explains the dynamical
802 pattern of paramyxoviruses. *Proceedings of the National Academy of Sciences*,
803 112(43):13396–13400, 2015.
- 804 [25] Virginia E Pitzer, Cécile Viboud, Wladimir J Alonso, Tanya Wilcox, C Jessica
805 Metcalf, Claudia A Steiner, Amber K Haynes, and Bryan T Grenfell. Environmental
806 drivers of the spatiotemporal dynamics of respiratory syncytial virus in
807 the United States. *PLoS pathogens*, 11(1):e1004591, 2015.
- 808 [26] Katharine R Dean, Fabienne Krauer, Lars Walløe, Ole Christian Lingjærde, Barbara
809 Bramanti, Nils Chr Stenseth, and Boris V Schmid. Human ectoparasites
810 and the spread of plague in Europe during the Second Pandemic. *Proceedings
811 of the National Academy of Sciences*, 115(6):1304–1309, 2018.
- 812 [27] Margarita Pons-Salort and Nicholas C Grassly. Serotype-specific immunity
813 explains the incidence of diseases caused by human enteroviruses. *Science*,
814 361(6404):800–803, 2018.
- 815 [28] Sarah Cobey and Edward B Baskerville. Limits to causal inference with state-
816 space reconstruction for infectious disease. *PloS one*, 11(12):e0169050, 2016.
- 817 [29] Public Health Agency of Canada. Respiratory virus detections in
818 Canada. 2024. <https://www.canada.ca/en/public-health/services/surveillance/respiratory-virus-detections-canada.html>. Accessed Sep
819 4, 2024.
- 820 [30] Centre for Health Protection. Detection of pathogens from respiratory specimens.
821 2024. <https://www.chp.gov.hk/en/statistics/data/10/641/642/2274.html>. Accessed Nov 20, 2024.
- 822 [31] Centre for Health Protection. Detection of gastroenteritis viruses from faecal
823 specimens. 2024. <https://www.chp.gov.hk/en/statistics/data/10/641/717/3957.html>. Accessed Nov 20, 2024.
- 824 [32] Korea Disease Control and Prevention Agency. Acute respiratory infection,
825 Sentinel surveillance infectious diseases. 2024. <https://dportal.kdca.go.kr/pot/is/st/ari.do>. Accessed Nov 20, 2024.

- 830 [33] Edward Goldstein, Sarah Cobey, Saki Takahashi, Joel C Miller, and Marc Lip-
831 sitch. Predicting the epidemic sizes of influenza A/H1N1, A/H3N2, and B: a
832 statistical method. *PLoS medicine*, 8(7):e1001051, 2011.
- 833 [34] Bob Carpenter, Andrew Gelman, Matthew D Hoffman, Daniel Lee, Ben
834 Goodrich, Michael Betancourt, Marcus A Brubaker, Jiqiang Guo, Peter Li,
835 and Allen Riddell. Stan: A probabilistic programming language. *Journal of*
836 *statistical software*, 76, 2017.
- 837 [35] Stan Development Team. RStan: the R interface to Stan, 2024. R package
838 version 2.32.6.